Alternative splicing modulates chromatin interactome and phase separation of the RIF1 C-terminal domain

Adenine Si-Hui Koo[1]†, Weiyan Jia[1]†, Sang Hwa Kim[1], Mark Scalf[2], Claire E. Boos[2], Yuhong Chen[3], Demin Wang[3,4], Andrew F. Voter[5], Aditya Bajaj[6], Lloyd M. Smith[2], James L. Keck[5], Christopher J. Bakkenist[7], Lin Guo[6], and Randal S. Tibbetts[1]*

[1]Department of Human Oncology
University of Wisconsin School of Medicine and Public Health
1111 Highland Ave
Madison, WI 53705, USA

[2]Department of Chemistry
University of Wisconsin-Madison
1101 University Ave
Madison, WI 53706, USA

[3]Versiti Blood Research Institute
Milwaukee, WI, 53226, USA

[4]Department of Microbiology and Immunology
Medical College of Wisconsin, Milwaukee, WI, 53226, USA

[5]Department of Biomolecular Chemistry
University of Wisconsin-Madison
420 Henry Mall
Madison, WI 53706, USA

[6]Department of Biochemistry and Molecular Biology
Thomas Jefferson University
Philadelphia, PA 19107, USA

[7]Department of Radiation Oncology
University of Pittsburgh
Pittsburgh, PA 15260, USA

†These authors contributed equally.

*Corresponding author. Tel: +1 608 262 0027; Fax: +1 608 262 3913; Email: rstibbetts@wisc.edu

ABSTRACT

RIF1 (RAP1 interacting factor) fulfills diverse roles in DNA double-strand break repair, DNA replication, and nuclear organization. RIF1 is expressed as two splice variants, RIF1-Long (RIF1-L) and RIF1-Short (RIF1-S), from the alternative splicing (AS) of Exon 32 (Ex32) which encodes a 26 aa Ser/Lys-rich cassette peptide in the RIF1 C-terminal domain (CTD). Here we demonstrate that Ex32 inclusion was repressed by DNA damage and oncogenesis but peaked

at G_2/M phase of the cell cycle. Ex32 splice-in was catalyzed by positive regulators including SRSF1, which bound to Ex32 directly, and negative regulators such as PTBP1 and SRSF3. Isoform proteomics revealed enhanced association of RIF1-L with MDC1, whose recruitment to IR-induced foci was strengthened by RIF1-L. RIF1-L and RIF1-S also exhibited unique phase separation and chromatin-binding characteristics that were regulated by CDK1-dependent CTD phosphorylation. These combined findings suggest that regulated AS affects multiple aspects of RIF1 function in genome protection and organization.

HIGHLIGHTS

1. RIF1 AS is dynamically regulated by DNA damage and cell cycle signaling.
2. RIF1-L to RIF1-S isoform switch is associated with primary cancers.
3. SRSF1 acts directly on Exon 32 to promote RIF1-L expression.
4. S/K cassette expanded the RIF1 chromatin interactomes and stabilized phase separation.

Graphical Abstract

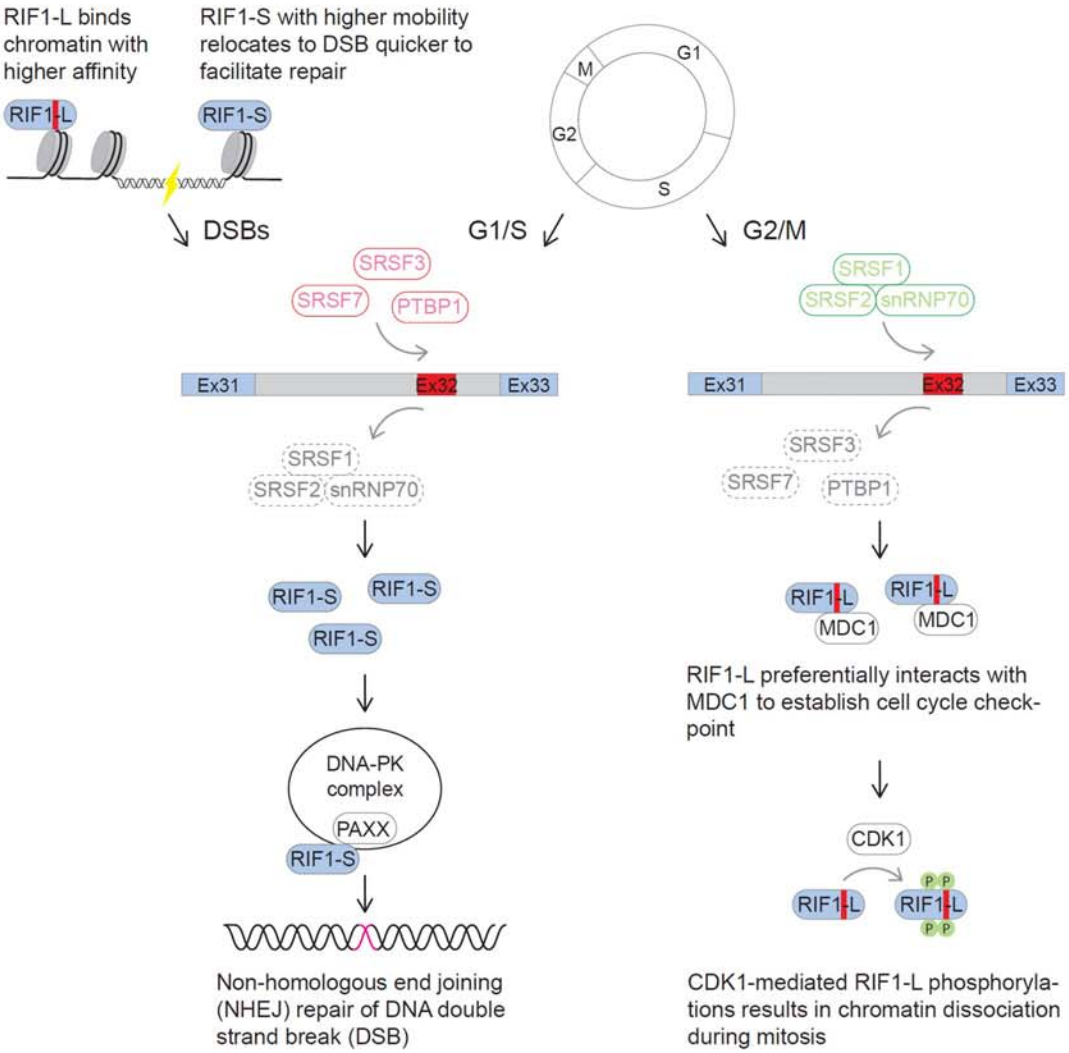

Highlights

1. RIF1 AS is dynamically regulated by DNA damage and cell cycle signaling.
2. RIF1-L to RIF1-S isoform switch is associated with primary cancers.
3. SRSF1 acts directly on Exon 32 to promote RIF1-L expression.
4. S/K cassette expanded the RIF1 chromatin interactomes and stabilized phase separation.

INTRODUCTION

Originally identified as a telomere-binding factor in *Saccharomyces cerevisiae*, the RIF1 (RAP1 interacting factor) gene encodes a ~270 kDa protein that fulfills diverse roles in eukaryotic genome maintenance [1,2]. In mammals, RIF1 functions downstream of the canonical H2A.X-MDC1-53BP1 signaling axis to influence DNA double-strand break repair (DSBR) pathway choice [3]. In G_1 and early S phase, 53BP1-dependent recruitment of RIF1 to DNA double-strand breaks (DSBs) promotes their repair via non-homologous end joining (NHEJ) while suppressing BRCA1-dependent homology-directed repair (HDR) [4-7]. Specifically, RIF1 recruits heterotrimeric Shieldin that suppresses 5' $\rightarrow$ 3' end resection to inhibit HDR [8-11]. RIF1-deficient cells phenocopy elements of 53BP1 deficiency, including NHEJ and class-switch recombination (CSR) defects, as well as the inappropriate recruitment of BRCA1 to DSBs in G_1 phase [4,12-14]. Furthermore, RIF1 deficiency rescues HDR defects and PARP inhibitor sensitivity of BRCA1-mutant cells, establishing RIF1 as a key player in 53BP1-dependent DSBR pathway choice [4,12].

RIF1 also executes several important roles in DNA replication control. RIF1 is a component of the Bloom's (BLM) helicase complex that suppresses deleterious end resection at stalled replication forks (RFs) to facilitate RF restart and recovery [15]. RIF1 also delays replication origin firing through the recruitment of protein phosphatase 1 (PP1) to late origins, leading to dephosphorylation of the MCM4 subunit of the replicative minichromosome maintenance (MCM) DNA helicase [16]. Therefore, RIF1-deficient cells exhibit delayed DNA replication rates, hypersensitivity to DNA replication inhibitors, and a defect in the IR-induced intra-S phase checkpoint [17,18].

Possibly independent of its proximal role in suppressing origin firing, RIF1 also regulates genome-wide DNA replication timing (RT) through its effects on nuclear architecture, in which it organizes chromatins into topologic domains with similar RT in early G_1 phase prior to the assembly of functional origin recognition complexes [19]. RIF1-deficient mammalian cells or yeasts exhibit spatial changes in DNA replication domains that correlate with premature replication origin firing [20-22] (reviewed in Ref.23). RIF1 chromatin occupancy correlates with the RT of individual chromatin domains suggesting RIF1's role in bundling co-regulated origins [24]. Interestingly, RIF1 participation in spatial organization of the replication domain is genetically separable from its participation in RT regulation [25]. Lastly, RIF1 also plays a role in the resolution of ultrafine DNA bridges in anaphase cells [26,27].

How RIF1 simultaneously mediates DSBR pathway choice, replication origin regulation, and nuclear architecture is unclear. RIF1 C-terminal domain (CTD) harbors a 26 aa Ser/Lys (S/K) cassette encoded by *RIF1*-Exon 32 (Ex32) that is subjected to alternative splicing (AS) to generate RIF1-Long (RIF1-L) and RIF1-Short (RIF1-S) isoforms [28]. RIF1 AS likely confers distinct functional properties to RIF1 isoforms through modular protein-protein interactions and posttranslational modifications.

Here we investigated the regulation and functional consequences of RIF1 AS using *RIF1*$^{-/-}$ U-2 OS cell lines expressing GFP-tagged RIF1-L or RIF1-S, and RIF1-L-deficient mice. We identified extracellular signals and a suite of RNA binding proteins (RBPs) responsible for RIF1 AS. We showed that the inclusion of the S/K cassette altered RIF1 chromatin interactome, enhanced RIF1 chromatin binding, and stabilized phase separation of the RIF1 CTD. Finally, we made the unexpected discovery that the S/K cassette, in conjunction with a downstream basic motif, confers selective microtubule association to RIF1-L. These studies illuminate mechanisms and functional consequences of RIF1 AS that may contribute to its diverse roles in genome stability.

MATERIAL AND METHODS

Cell culture and treatment

U-2 OS, HeLa, H460, and HEK293T cell lines were obtained from the American Type Culture Collection (ATCC). U-2 OS and its derivative cell lines were grown in McCoy's 5A medium (Corning, 10-050-CV). HEK293T and HeLa cells were grown in DMEM medium (Corning, 10-013-CV). All cell lines were grown in medium supplemented with 10% fetal bovine serum (Atlanta biologicals) and 1% Penicillin/Streptomycin (Corning, 30-002-CI) and incubated at 37^{o}C in 5% CO_2. For G_1/S synchronization experiments, cells were treated with 2 mM thymidine for 19 h, released into thymidine-free growth media for 9 h, and then returned to thymidine-containing media for an additional 16 h [29]. The cells were washed three times with PBS, and then released into complete media for the indicated time periods. Calicheamicin γ1 (CLM) was prepared at a concentration of 4 µM stock solution in DMSO and used at a concentration of 2-10 ng/ml for 4-6 h. For checkpoint inhibitor treatments, U-2 OS cells were treated with 5 µM AZD6738 (ATRi), 2 µM BAY1895344 (ATRi) or 0.5 µM AZD1775 (Wee1i) diluted in DMSO for 1, 2 or 4 hours prior to harvesting.

Gene editing and cloning

RIF1$^{-/-}$ and *RIF1*$^{\Delta Ex32}$ cells were generated by transient transfection of U-2 OS cells with pX459 vectors (v2, Addgene plasmid #62988) [30,31] harboring two sgRNA sequences targeting RIF1-Ex2 (5'-CACCgAGTCTCCAACAGCGGCGCGA-3' and 5'-AAACTCGCGCCGCTGTTGGAGACTc-3') or RIF1-Ex32 (5'-CACCgATTTAGGGCTACGTGATCCT-3' and 5'-AAACAGGATCACGTAGCCCTAAATc-3') using jetPRIME (Polyplus, 114-07). Twenty-four hours after transfection, cells were selected for 72 h with 1 µg/ml puromycin and then diluted into 96-well-plates at an average density of 1 cell per well. Each single clone was isolated and screened for RIF1 knockout phenotype through immunostaining of ionizing radiation-induced foci (IRIF) and Western blotting with α-RIF1 and α-RIF1-L antibodies. All clones were sequenced around the sgRNA targeted sequence, and five clones (*RIF1*$^{-/-}$: H1 and 2C5; *RIF1-L*$^{-/-}$: A6, 2A2, and H11) were selected for further study.

We reconstituted *RIF1*$^{-/-}$ U-2 OS cells with full-length RIF1-L and RIF1-S coding sequences (CDS) cloned into a tetracycline-inducible pcDNA5-eGFP-FRT/TO plasmid vector (Addgene plasmid #19444) by Gateway recombination cloning (Invitrogen, 11789020 and 11791020) [6]. Resulting GFP-RIF1-L and GFP-RIF1-S plasmids were cotransfected into *RIF1*$^{-/-}$ Tet-on U-2 OS cells with pOG44 using JetPrime, selected with 200 µg/ml hygromycin for one week, and tested for RIF1 expression following induction with 1 µg/ml doxycycline (Dox). GFP plasmid was included as a control. The three resulting cell lines, *RIF1*$^{-/-}$:GFP, *RIF1*$^{-/-}$:GFP-RIF1-L and *RIF1*$^{-/-}$:GFP-RIF1-S are also being referred as GFP, GFP-RIF1-L and GFP-RIF1-S expressing cells throughout this paper. *RIF1*$^{-/-}$ U-2 OS cells expressing GFP-tagged RIF1^{CTD} constructs were generated by PCR amplifying codons 2170-2472 of the RIF1-L or RIF1-S CDSs followed by Gateway cloning into pcDNA5-eGFP-FRT/TO. Point mutations were introduced through QuikChange mutagenesis method and all constructs were sequenced in their entirety. GFP-RIF1-L^{CTD} and GFP-RIF1-S^{CTD} constructs were stably transfected into *RIF1*$^{-/-}$ U-2 OS cells as described above. Experimentally verified CDK1 phosphorylation sites of human RIF1 protein was queried from UniProt website under the primary accession ID: Q5UIP0 on 6th July 2022.

RNA extraction, RIF1 splicing assay, and quantitative PCR (qPCR)

Total RNA was extracted in TRIzol reagent (Invitrogen, 15596018) followed by cDNA synthesis by iScript™ cDNA Synthesis Kit (Bio-Rad, 1708891) according to manufacturer's protocols.

Human *RIF1*-Ex32 splicing was evaluated by RT-PCR using primers located in Ex31 and Ex33 (RIF1-Ex31-F: 5'-AAGCAGGATTGGCAGATGAC-3' and RIF1-Ex33-R: 5'-GATGTCAACTGGTGCCACAC-3'). Positionally analogous primers located within mouse *Rif1*-Ex31 (5'-AAGCAGGATTGGCAGATGAC-3') and Ex33 (5'-GATGTCAACTGATGCTGCAC-3) were used to analyze mouse *Rif1*-Ex32 splicing. Primers flanking Ex1a (RIF1-Ex1a-F: 5'-CGCCATCTTGGTCTAGGAGG-3' and RIF1-Ex1a-R: 5'-ACGACTGGTCAGAGTCAGGT-3') were used as a negative control. Beta-actin (Actin-F: 5'-TCCCTGGAGAAGAGCTACG-3' and Actin-R: 5'-GTAGTTTCGTGGATGCCACA-3') or GADPH (GAPDH-F: 5'-AATCCCATCACCATCTTCCA-3' and GAPDH-R: 5'-TGGACTCCACGACGTACTCA-3') was used as an internal control. RIF1 AS leads to the formation of RIF1-L and RIF1-S transcripts with a length difference of 78 nt which can be resolved subsequently by 2% w/v agarose gel electrophoresis (See Fig. 1B).

RIF1 isoform specific qPCR in human cells was performed using the following primers: RIF1-L (5'-GGATTGGCAGATGACATTGATAGA-3'; 5-TCCTTTGGCTGAAGTGGTATTATG-3'); RIF1-S (5'-CCTACTACACAATCTAAGATTTCA-3'; 5'-GCTCTAATGAGTTGTCCCA-3'); and total RIF1 (5'-CGCTGTGTCTGGTCTCCTT-3'; 5'GCACCGTCTATCAATGTCATCTG-3').

RNAi and shRNA screening

siRNA screen for RIF1 splicing regulators was performed through a SMARTpool siRNA library (Dharmacon) targeting 151 RNA binding proteins in the human genome that was obtained through UW Small Molecule Screening & Synthesis Facility (SMSSF) [32]. Approximately 10,000 HeLa cells were reverse-transfected with 20 nM of each of the siRNAs using DharmaFECT1 (Dharmacon) in 96-wells plates for a 48-hour period. Subsequently, the transfected cells were lysed in TRIzol reagent for RNA extraction, and cDNA was synthesized as described. RIF1 splicing assay was performed as described to identify candidate RIF1 splicing factors.

The following shRNA lentiviral vectors targeting candidate RIF1 splicing regulators were purchased from Sigma: SRSF1 (cat# TRCN0000001095); SRSF2 (cat# TRCN0000000084); SRSF3 (cat# TRCN0000001227); SRSF7 (cat# TRCN0000001142); PTBP1 (cat# TRCN0000231420); RBM28 (cat# TRCN0000239461); and snRNP70 (cat# TRCN0000000011). Lentiviral particles were produced by transient transfection of HEK293T cells with shRNA vectors, psPAX2 (Addgene plasmid #12260) and pCMV-VSV-G (Addgene plasmid #8454) in a ratio of 3:2:1 as described [29,33]. Viral supernatants harvested at 24 h and 48 h post-transfection were incubated with U-2 OS cells for 24 h followed by selection in media containing 2 µg/ml puromycin for 72 h. Cells were harvested in TRIzol reagent for RIF1 splicing assays.

RNA immunoprecipitation (RNA-IP)

Approximately 50 million cells were lysed in 1 mL ice-cold NET-2 buffer (50 mM Tris-HCl (pH 7.5), 150 mM NaCl, 0.05% v/v NP40) supplemented with 2 mM 1,4-dithiothreitol, 0.2 U/µL RNasin Plus (Promega, N2611), 20 mM sodium fluoride, 20 mM β-glycerophosphate and 2X protease inhibitor cocktail (Sigma, P8340-5ml; Thermo Scientific, 78438). The lysate was sonicated using five pulses of 3 s ON, 30 s OFF followed by three pulses of 10 s ON and 30 s OFF at an amplitude of 30% (Fisher Scientific, FB120). The supernatant was incubated with 5 µg of either the targeted antibodies (SRSF3: Cell Signaling Technology #35073; SRSF7: Bethyl A303-772A; PTBP1: ThermoFisher, 32-4800; SRSF1-M: Santa Cruz, sc33652; SRSF1-R: abcam, ab38014; SRSF2: Proteintech 20371-1-AP; snRNP70: Invitrogen #PA5-115943) or normal IgG controls (Mouse: Millipore, 12-371; Rabbit: Millipore, 12-370) for 1 h on a nutator mixer at 4°C before Protein A/G PLUS-Agarose bead suspension (Santa Cruz, sc-2003) was added (20 µl/1 µg of antibody) for overnight incubation. The beads were washed with NET-2 buffer five times and the immunoprecipitated RNA was extracted by TRIzol reagent. Relative

fold enrichment of RIF1 pre-mRNA in the target RNA-IP sample versus the control IgG sample was quantified by qPCR assay with two pairs of intron-exon primers. Primer set 1 (PS1) targets RIF1-In31 and RIF1-Ex32 while primer set 2 (PS2) targets RIF1-Ex32 and RIF1-In32 (RIF1-In31-F: 5'-TAGTCATCTAGGGTTCTGAGTG-3' and RIF1-Ex32-R: 5'-TCCTTTGGCTGAAGTGGTATTATG-3'; RIF1-Ex32-F: 5'-CATAATACCACTTCAGCCAAAGG-3' and RIF1-In32-R: 5'- GTGACATGAAAACTAAAGCACTTC-3').

EdU labeling, flow cytometry, and immunofluorescent microscopy

For cell cycle progression experiments, U-2 OS cells were incubated with 20 µM 5-ethynyl-2'-deoxyuridine (EdU) for 30 min before collection and then fixed with ice-cold 70% ethanol. EdU detection was performed using the Click-IT Plus EdU Alexa Fluor 647 Flow Cytometry Assay Kit (Life Technologies, C10634). Propidium iodide (PI) was added at a concentration of 50 µg/ml. Flow cytometry was performed on Thermo Fisher Attune, and data was analyzed and organized using FlowJo software. For *in situ* EdU and 5-bromo-2′-deoxyuridine (BrdU) staining, U-2 OS cells were pulse labelled with 20 µM BrdU or EdU for 30 min and fixed with 4% w/v paraformaldehyde (PFA). For BrdU detection, cells were then incubated with 2 M HCl for 30 min and then permeabilized with 0.2% v/v Triton X-100 for 15 min at room temperature, washed and blocked in 3% w/v bovine serum albumin (BSA). Cells were stained with BrdU primary antibody (Santa Cruz, sc-32323) in 3% BSA and incubated overnight at 4^{o}C, followed by washing in 0.02% v/v PBST (PBS with 0.02% v/v Tween-20) and incubation with appropriate secondary antibodies in 3% BSA for 1 h at room temperature. EdU was detected by click chemistry as described above. Samples were mounted in VECTASHIELD mounting medium with DAPI (Vector, H-1200) before imaging.

For immunostaining experiments, cells were seeded into 12-well plate with glass coverslips, fixed with 4% w/v PFA, permeabilized with 0.2% v/v Triton X-100 and blocked with 3% w/v BSA at room temperature. The coverslips were then transferred to an improvised humidity chamber for immunostaining with the appropriate primary antibodies at 37°C for an hour or at 4°C overnight. The source and the dilution factor of the antibodies used were indicated here: MDC1 (Sigma HPA006915, 1:500); α-tubulin (Sigma T6199, 1:500). Coverslips were washed 3 X 10 min with 0.05% v/v PBST (PBS with 0.05% v/v Tween-20) before incubating with Alexa Fluor™ secondary antibodies (Thermo Fisher #A11032, #A32733) at a dilution factor of 1:10,000 at room temperature for 45 min. Coverslips were washed 3 X 10 min with 0.05% PBST followed by 2 X 1 min with PBS before mounting. Nuclear DNA was either stained with 0.5 µg/ml DAPI for 10 min at room temperature and then mounted with mounting medium for fluorescence (Vector, H-1000), or directly mounted in mounting medium with DAPI for fluorescence (Vector, H-1200) before imaging. Images were acquired using Nikon A1RS or Nikon AX confocal microscopes under the desired objectives. Images were organized using NIS-Elements Advanced Research/Fiji software. Foci counts were done in CellProfiler (version 4.2.6). Anisosome area measurement was performed in Fiji through Labkit classifier followed by manual annotation. For immunostaining of microtubules (MTs), *RIF1*$^{-/-}$ U-2 OS cells expressing GFP, GFP-RIF1-L, or GFP-RIF1-S, were pre-extracted for 5 min with cytoskeleton (CSK) buffer (20 mM HEPES-KOH (pH 7.4), 3 mM $MgCl_2$, 300 mM sucrose) containing 100 mM NaCl and 0.5% v/v Triton X-100 at 4°C to reduce cytoplasmic background signal and induce MTs depolymerization prior to cell fixation and permeabilization.

DNA replication pattern analysis

DNA replication pattern analyses were performed as described [29]. *RIF1*$^{-/-}$, *RIF1*$^{-/-}$:GFP, *RIF1*$^{-/-}$:GFP-RIF1-L, and *RIF1*$^{-/-}$:GFP-RIF1-S U-2 OS cells were pulse labeled with EdU for 20 min and stained for EdU incorporation. The presence of early, mid, or late DNA replicative stages were accessed from the EdU staining patterns. The percentages were calculated for each sample.

Alternatively, cells were synchronized with 2 mM thymidine for 19 h, released into thymidine-free growth media for 9 h, and then returned to thymidine-containing media for 6 h, at which time most cells are in mid-S phase [29]. Cells were then pulse labeled with EdU as described [29]. A minimum of 100 cells per sample was imaged by confocal microscopy.

Protein extraction, chromatin fractionation and immunoblotting

For whole-cell protein extraction, cells were lysed in either high salt lysis buffer (50 mM Tris, pH 7.5, 300 mM NaCl, 10% glycerol, 2 mM $MgCl_2$, 3 mM EDTA, and 0.5% Triton X-100) or modified RIPA buffer (50 mM Tris-HCl, pH 7.4, 150 mM NaCl, 1 mM EDTA, pH 8, 1% sodium deoxycholate, 0.1% SDS, and 1% Triton X-100) supplemented with 10 mM sodium fluoride, 10 mM β-glycerophosphate and 1X Protease Inhibitor Cocktail (Sigma, P8340-5ml; Thermo Scientific, 78438). The lysate was incubated on ice for 10 min and sonicated using 5 pulses of 3 s ON, 5 s OFF at an amplitude of 30% (Fisher Scientific, FB120) before the addition of 4X SDS sample buffer (200 mM Tris-HCl (pH 6.8), 40% glycerol, 8% SDS, 0.5% bromophenol blue and 10% beta-mercaptoethanol). The samples were heated at 95^{o}C for 5 min prior to freezing at -20°C for storage or loading directly for immunoblotting.

For chromatin fractionation of full-length RIF1, cells were resuspended in CSK buffer containing 150 mM NaCl and 0.5% Triton X-100 supplemented with 20 mM sodium fluoride, 20 mM β-glycerophosphate and 2X Protease Inhibitor Cocktail. The cells were incubated on ice for 20 min. Fifty percent of the cell suspension was kept as whole cell extract (WCE) with the addition of 50 U/ml Benzonase (Sigma, E1014-5KU) followed by a 20 min on-ice digestion. The remaining cell suspension was centrifuged for 5 min at 5,000 x *g* at 4^{o}C. The supernatant was transferred to a new tube and saved as the soluble fraction (SF) which contains cytoplasmic and nucleoplasmic content, while the pellet/chromatin fraction (CF) was washed twice in CSK buffer without detergent and resuspended in complete CSK buffer with 50 U/ml Benzonase for a 20 min on-ice digestion. All lysates were mixed with 0.5 v/v of 4X SDS sample buffer and heated at 95^{o}C for 15 min before loading. Chromatin fractionation of the RIF1 CTD constructs was done with the same procedure, but the salt concentration of the CSK buffer was reduced to 100 mM due to higher solubility of RIF1 CTD compared to full-length RIF1.

For immunoblotting, samples were separated by 6% or 12% SDS-polyacrylamide gel (SDS-PAGE) depending on the molecular weight of the target protein and transferred to 0.45 µm Immobilon®-FL PVDF Membrane (Millipore, IPFL00010). The membranes were blocked with blocking solution (5% w/v milk in Tris-buffered saline, 0.1% v/v Tween 20 (TBST)) for an hour before blotting with target primary antibodies overnight at 4°C. The source and the dilution of the primary antibodies used were listed as followed: Total RIF1 (Bethyl Laboratories A300-569A; 1:500); GFP (Santa Cruz sc9996, 1:200); MCM2 (Santa Cruz sc373702, 1:100); MCM4 (Abcam ab4459, 1:1000); vinculin (Santa Cruz sc73614, 1:100); lamin B1 (Abcam ab16048, 1:2000); beta-tubulin (Sigma Millipore 05-661, 1:1000). After that, the membranes were washed 3 X 5 min with TBST and incubated with LI-COR IRDye secondary antibodies (IRDye 800CW goat anti-rabbit or IRDye 680RD goat anti-mouse) at a dilution of 1:10000 in blocking solution for an hour at room temperature. Membranes were washed 3 X 5 min with TBST and images were acquired using Odyssey Fc (LI-COR Biosciences). The exported images were then analyzed and organized with ImageStudio software (v5.2, LI-COR Biosciences).

RIF1 isoform-specific antibodies

α-RIF1-L, α-RIF1-S, and α-RIF1-pS2260/65 antibodies (Lifetein, LLC) were peptide-affinity purified from the sera of rabbits injected with the following KLH-conjugated immunogens, respectively: hRIF1-S (N-VKTSPTTQSKISEMAKESIP-C); hRIF1-L (N-AKGFLSPGSRSPKFKSSKKC-C); RIF1-pS2260/65 (N-AKGFL[pS]PGSRPKFKSSKKC-C). α-

RIF1-pS2260/65 antisera were first immunodepleted against an identical non-phosphorylated peptide prior to affinity purification using the phosphopeptide. All antibodies were used at a dilution of 1:500 for Western blotting and immunofluorescence staining experiments.

RIF1 purification and mass spectrometry (MS)

RIME (rapid immunoprecipitation mass spectrometry of endogenous proteins) assay of GFP-RIF1-L and GFP-RIF1-S expressed on a *RIF1*$^{-/-}$ background was carried out as described [29,34]. Briefly, ~20 million cells were counted and fixed with 20 ml 1% formaldehyde solution for 8 minutes at room temperature. Fixation was quenched by adding 0.12 M glycine. The soluble fraction was extracted in 10 ml of LB1 (50 mM HEPES-KOH (pH 7.5), 140 mM NaCl, 1 mM EDTA, 10% Glycerol, 0.5% NP-40, 0.25% Triton X-100, 1X Protease Inhibitor Cocktail (Sigma, P8340-5ml) for 10 min with rotation at 4^{o}C. Cell nuclei were pelleted and washed once with 10 ml LB2 (10 mM Tris-HCl (pH 8.0), 100 mM NaCl, 1 mM EDTA, 0.5 mM EGTA, 1X Protease Inhibitor Cocktail) and then resuspended in 500 µl LB3 (10 mM Tris-HCl (pH 8.0), 100 mM NaCl, 2.5 mM $MgCl_2$, 0.1% w/v sodium deoxycholate, 0.5% Triton X-100, 1X Protease Inhibitor Cocktail) with 500 U Benzonase and incubated at room temperature for 30 min. Benzonase was deactivated with 2 mM EDTA and 1 mM EGTA. The mixture was supplemented with 50 µl 10% Triton X-100 and 37.5 µl of 4 M NaCl before LB3 was added to bring the total lysate volume of each sample to 1 ml. Digested lysates were sonicated for 3 pulses of 10 s ON, 50 s OFF at an amplitude of 40% and clarified by centrifugation at 20,000 x *g* for 10 min at 4^{o}C. The supernatants were incubated with ChromoTek GFP-Trap Magnetic Agarose beads (Fisher Scientific) per manufacturer's recommendations on a nutator mixer at 4^{o}C overnight. Subsequently, 50 µl of pre-washed Dynabeads protein G (Invitrogen, 10003D) was added to the lysates and incubated for additional 4 h at 4^{o}C.

For Western blotting, beads were washed sequentially with 1 ml LB3 and 1 ml RIPA buffer (50 mM HEPES-KOH (pH 7.5), 0.5 M LiCl, 1 mM EDTA, 1% NP-40, 0.7% w/v sodium deoxycholate, 1X Protease Inhibitor Cocktail) once and boiled in 100 µl 2X SDS sample buffer. For mass spectrometry, beads were washed 5 times with 1 ml of RIPA buffer and twice in 1 ml of cold freshly prepared 100 mM ammonium hydrogen carbonate (AMBIC) solution and processed as described [34].

GFP-RIF1 RIME IPs were subjected to tryptic digestion and LC-MS/MS analysis using an Orbitrap Fusion™ Lumos™ Tribrid™ mass spectrometer using the filter aided sample preparation (FASP) method [35]. The tryptic digest solution was desalted/concentrated using an Omix 100 µL (80 µg capacity) C18 tip. The solution was pipetted over the C18 bed 5 times, and rinsed 3 times with H_2O, 0.1% trifluoroacetic acid (TFA) to desalt. The peptides were eluted from the C18 resin into 150 µL 70% acetonitrile, 0.1% TFA and lyophilized. The peptides were re-suspended in 95:5 H_2O:acetonitrile, 0.2% formic acid and analyzed in duplicate as described below. Samples were analyzed using a UPLC-MS/MS system consisting of an Easy-nLC 1200 ultra-high-pressure liquid chromatography system and an Orbitrap Fusion Lumos mass spectrometer (ThermoFisher Scientific). Peptides were loaded in buffer A (H_2O, 0.2% formic acid) at a pressure of 300 Bar onto a 20-cm-long fused silica capillary nano-column packed with C18 beads (1.7 µm-diameter, 130 Angstrom pore size from Waters). Peptides eluted over 120 minutes at a flow rate of 350 nL/min with the following gradient established by buffer A (H_2O, 0.2% formic acid) and buffer B (80% acetonitrile (ACN), 0.2% formic acid): Time/T = 1 mins, 5% buffer B; T = 52 mins, 30% buffer B; T = 80 mins, 42% buffer B; T = 90 mins, 55% ACN; T = 95 to 100 mins, 85% buffer B; T = 101 to 120 mins, equilibrate at 0% buffer B. The nano-column was held at 60°C using a column heater (in-house constructed) [36].

The nanospray source voltage was set to 2200V. Full-mass profile scans were performed in the orbitrap between 375-1500 m/z at a resolution of 120,000, followed by MS/MS HCD scans in the orbitrap of the highest intensity parent ions in a 3 seconds cycle time at 30% relative collision energy and 15,000 resolution, with a 2.5 m/z isolation window. Charge states 2-6 were included and dynamic exclusion was enabled with a repeat count of one over a duration of 30 seconds and a 10 ppm exclusion width both low and high. The AGC target was set to "standard", maximum inject time was set to "auto", and 1 µscan was collected for the MS/MS orbitrap HCD scans.

The MetaMorpheus software program was used to identify peptides and proteins in the samples [37,38]. Protein fold changes were normalized and quantified from two technical replicates for each of the three biological replicates by FlashLFQ [39,40].

Proximity-ligation assay (PLA)

RIF1$^{-/-}$ U-2 OS cells expressing GFP, GFP-RIF1-L, or GFP-RIF1-S were mock irradiated or exposed to 10 Gy IR followed by 2 h recovery. The cells were then pre-extracted for 8 min with CSK buffer containing 100 mM NaCl and 0.5% v/v Triton X-100 to reduce cytoplasmic background signal prior to cell fixation and primary antibodies incubation (α-GFP, Santa Cruz sc9996, 1:250; α-MDC1, Sigma HPA006915, 1:500) overnight. Reagent kits for Duolink® Proximity Ligation Assay (Sigma) were used and PLA was performed according to the manufacturers' conditions.

Fluorescence recovery after photobleaching (FRAP)

U-2 OS cells were seeded in 38 mm glass bottom dishes and transfected at 60-80% confluency with 2.5 µg of GFP-RIF1^{CTD} plasmid using Lipofectamine 3000 (ThermoFisher, L3000015) in 7.5 µL Lipofectamine and 5 µL P3000 reagents, each diluted in 120 µL serum-free McCoy's 5A medium. The transfection medium was changed 4 h post-transfection and the cells were incubated overnight for transgene expression. FRAP was carried out with ND Stimulation module (Nikon NIS-Elements AR) on Nikon AX confocal microscope 24 hours post-transfection with 25% 488 nm laser for 1.02 s on anisosomes of roughly 2.5 nm in diameter. Recovery images were acquired at 5 s interval for 3 min post-bleaching. The resulting videos were analyzed in MATLAB scripts (https://github.com/adenine-koo/FRAP.git) according to the easyFRAP pipeline [41]. Briefly, the average pixel values of three regions of interest (nucleus, bleached anisosome, and background) were extracted. Frame stabilization of the bleached anisosome was performed based on a correlation algorithm. Full scale normalization was done to correct background fluctuation, starting intensity difference, acquisition bleaching/laser fluctuation as well as variation in bleaching depth. Each recovery curve was plotted and fitted by a single exponential equation to estimate its t-half value and mobile fraction.

***In vitro* phase separation assay**

RIF1-L and RIF1-S CTD fragments were subcloned into pDEST15 for expression as glutathione-S-transferase (GST) fusion proteins. GST-tagged RIF1 CTD fragments were transformed into BL21-AI strain. Protein expression was induced by growing the transformed bacteria in TB medium supplemented with 1 mM IPTG + 0.2% w/v arabinose and grown at 16°C overnight. Cells were then lysed in lysis buffer (50 mM HEPES pH 7.5, 300 mM NaCl, 1 mM DTT, 100 mM dextrose, 10% glycerol, 1X Protease Inhibitor Cocktail) by sonication. The soluble fractions were collected by centrifugation at 20,000 x g for 30 minutes at 4°C. The proteins were purified with GS4B resin and eluted in GS4B elution buffer (20 mM HEPES pH 7.4, 300 mM NaCl, 10% glycerol, 20 mM reduced glutathione, 200 mM trehalose). Purified GST-RIF1CTD-L and GST-RIF1CTD-S were then subjected to phase separation assays in the presence of 10% dextran/polyethylene glycol (PEG) as described [42]. Images were collected at 10 min post-mixing.

In vitro DNA binding assay

Fluorescein-labelled antiparallel G4 DNA (5□-FAM-TTT TTT GGG GGG GGG GGG GGG GGG GG-3□) was folded in refolding buffer (1 µM DNA, 10 mM Tris□HCl (pH 7.5), 50 mM KCl, 1 mM ethylenediaminetetraacetic acid (EDTA), 40% v/v polyethylene glycol 200), by heating to 95°C for 10 minutes and subsequent cooling over 4 hours. Purified RIF1 CTD was incubated with 5 nM DNA in reaction buffer (20 mM HEPES (pH 7.6), 50 mM KCl, 1 mM EDTA, 0.01% v/v Triton X-100, 10 % v/v polyethylene glycol 200) for 30 minutes at 30 °C. The fluorescence anisotropy of each sample was measured at 25°C with a Beacon 2000 fluorescence polarization system.

Generation of RIF1-L-deficient mice

One-cell embryos from C57BL/6J mice were injected with a mixture of 40 ng/µl of Cas9 protein (PNA Bio) and 25 ng/µl of each of the two sgRNAs complementary to the 3' portion of Rif1-In31 (sgRNA1: CCTAACATTTTACAAGGGCGATT) and 5' portion of Rif1-Ex32 (sgRNA2: CCCAGGATCACAGAGCTCTAAAT) of the m*Rif1* gene spanning nucleotides 51962725 to 52016781 of mouse chromosome 2 (Reference GRCm39 C57BL/6J). The region flanked by sgRNA1 and sgRNA2 comprised of 149 nt that includes Rif1-Ex32 5' splice acceptor (SA) site. Tail DNA from founder mice was subjected to deep sequencing using m*Rif1* primers and those mice exhibiting *Rif1* mutations were backcrossed to wild-type mice to obtain germline m*Rif1* mutant lines. Two lines were selected to be used in this study: a $Rif1^{iA}$ line harboring a single nucleotide (A) insertion at codon 2010 that likely reflects cleavage and error-prone repair at sgRNA2, and a $Rif1^{\Delta Ex32}$ line harboring a 129 nt deletion between sgRNA1 and sgRNA2 that deletes the 3'portion of intron 31 and the 5' portion of Ex32, including the 5' SA site. Analysis of T and B cell development, mitogenesis, and *in vitro* class switch recombination (CSR) were carried out using cells isolated from bone marrow and spleen of 6-8-week old $Rif1^{+/+}$ and $Rif1^{\Delta Ex32/\Delta Ex32}$ mice as previously described [43,44].

Statistical processing

Statistical analysis information including individual biological and technical replicates number, mean or median, and error bars are explained in the figure legends. Statistical tests were performed in Prism (v10, GraphPad) or R. The tests performed and the resulting *P* values are listed in the figure legends and/or figure panels.

RESULTS

RIF1 undergoes DNA damage and cell cycle dependent AS

The human RIF1 is a 2472 aa protein, approximately 270 kDa (Fig. 1A). The N-terminus comprises of an array of 21 folded HEAT (Huntingtin, elongation factor 3 (EF3), protein phosphatase 2A alpha subunit and yeast PI3K TOR1) repeats that exhibits phosphorylation dependent binding to 53BP1, recruits Shieldin3, and mediates RIF1 recruitment to IR-induced foci (IRIF) [45] (1 – 935 aa) (Fig. 1A). The partially folded C-terminal domain (CTD) (2170 – 2472 aa) consists of a nuclear localization signal (NLS) and three evolutionarily conserved regions (CR1 – CR3) based on sequence identity amongst vertebrate RIF1 proteins (Fig. 1A). CR2 additionally bears homology to the CTD of bacterial RNA polymerase α subunits (αCTD) [15]. RIF1 CTD mediates oligomerization, DNA binding, PP1 recruitment (through RVSF motif in CR1), and association with the BLM complex [15,45-49] (Fig. 1A).

RIF1 is expressed as two splice variants, RIF1-L and RIF1-S, that differ by the absence or presence of Exon 32 (Ex32), which encodes a 26 aa peptide that we have dubbed the S/K

cassette owing to the predominance of Ser and Lys residues (Fig. 1A). RT-PCR analyses using primers flanking Ex32 (Fig. 1B) revealed that RIF1-L (the 2472 aa isoform), was the major mRNA species in H-460, U-2 OS, and HEK293T cells while RIF1-S (the 2446 aa isoform), was slightly more abundant in HeLa cells (Fig. 1C). Cellular exposure to the radiomimetic drug Calicheamicin γ1 (CLM) increased relative abundance of the RIF1-S isoform in all four cell lines suggesting that DNA double-strand breaks (DSBs) repress Ex32 inclusion and promote the formation of RIF1-S (Fig. 1C). The decreased abundance of RIF1-L over the same time suggests this isoform may be selectively degraded under conditions of DNA damage. By contrast, the AS of a cassette exon in the Ubiquitin E3 ligase TRIP12 was not inhibited following CLM exposure in U-2 OS cells (Fig. 1D). Ex32 exclusion and repressed RIF1-L transcript production was CLM dose dependent and reached a maximum at 4-6 hours after treatment in U-2 OS and HeLa cells respectively (Fig. 1E,F). Ionizing radiation (IR) dose-dependently promoted Ex32 skipping in H460 cells, indicating that Ex32 exclusion is a general response to DNA damage (Fig. 1G,H). RIF1 AS also fluctuated during the cell cycle, with the highest RIF1-L/RIF1-S mRNA ratio in G_2/M-phase and the lowest ratio in G_1-phase HeLa cells (Fig. 1I,J).

We tested the impacts of canonical DNA damage repair (DDR) inhibitors on CLM-dependent Ex32 skipping. While RIF1-L/RIF1-S ratios were comparable between CLM-treated cells with vehicle, PARP, or ATM inhibitors, the combination of CLM and a DNA-PK inhibitor potentiated Ex32 skipping, which may be indicative of enhanced DSB induction (Sup. Fig. 1A,B). The combined findings indicate that RIF1 Ex32 splicing is dynamically regulated by genotoxic stress and during the cell cycle.

Koo *et al.* Fig. 1

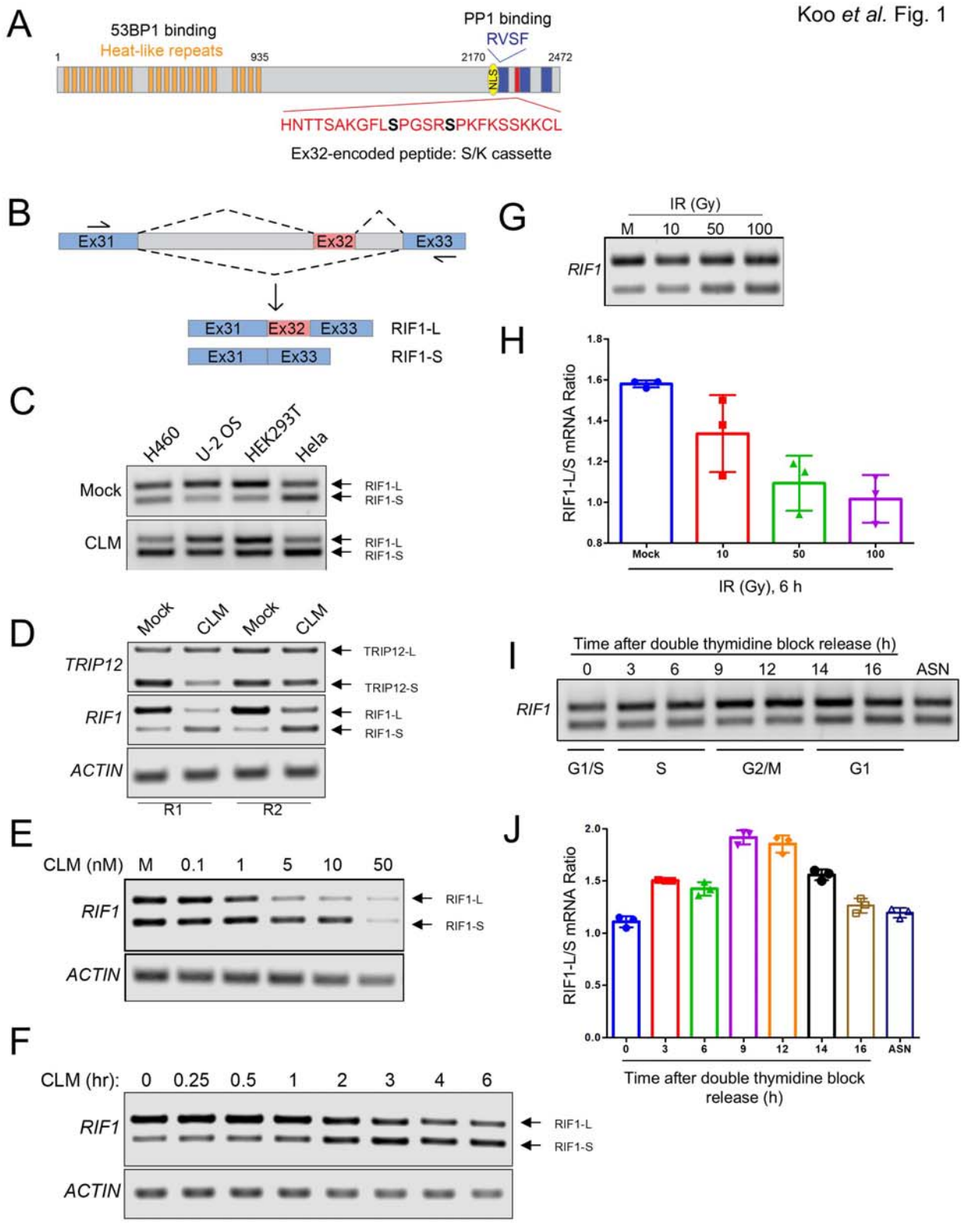

RIF1 isoform usage is altered in cancer

We queried publicly available RNA-Seq data from The Cancer Genome Atlas (TCGA) to estimate the abundance of RIF1-L and RIF1-S transcripts in normal versus tumor tissue across four selected cancer types by IsoformSwitchAnalyzeR [50] (Fig. 2A). Total RIF1 mRNA expression was significantly downregulated in breast invasive carcinoma (BRCA) relative to the matched normal breast tissue, while RIF1 expression levels were relatively upregulated in colon adenocarcinoma (COAD), lung adenocarcinoma (LUAD), and lung squamous carcinoma (LUSC) (Fig. 2B). When focusing on isoform levels, RIF1-S mRNA expression was significantly upregulated in BRCA, COAD, LUAD, and LUSC while RIF1-L expression was only significantly downregulated in BRCA but remained unchanged in COAD, LUAD, and LUSC (Fig. 2C). Strikingly, the usage of RIF1-S and RIF1-L isoforms in all four cancer subtypes showed the same trends: RIF1-S isoform usage was significantly increased, while RIF1-L isoform usage was significantly decreased, except in COAD, where RIF1-L isoform usage was slightly reduced, though not statistically significant (Fig. 2D). These findings suggest that RIF1 isoform switch from RIF1-L to RIF1-S may be associated with primary cancers.

Koo *et al.* Fig. 2

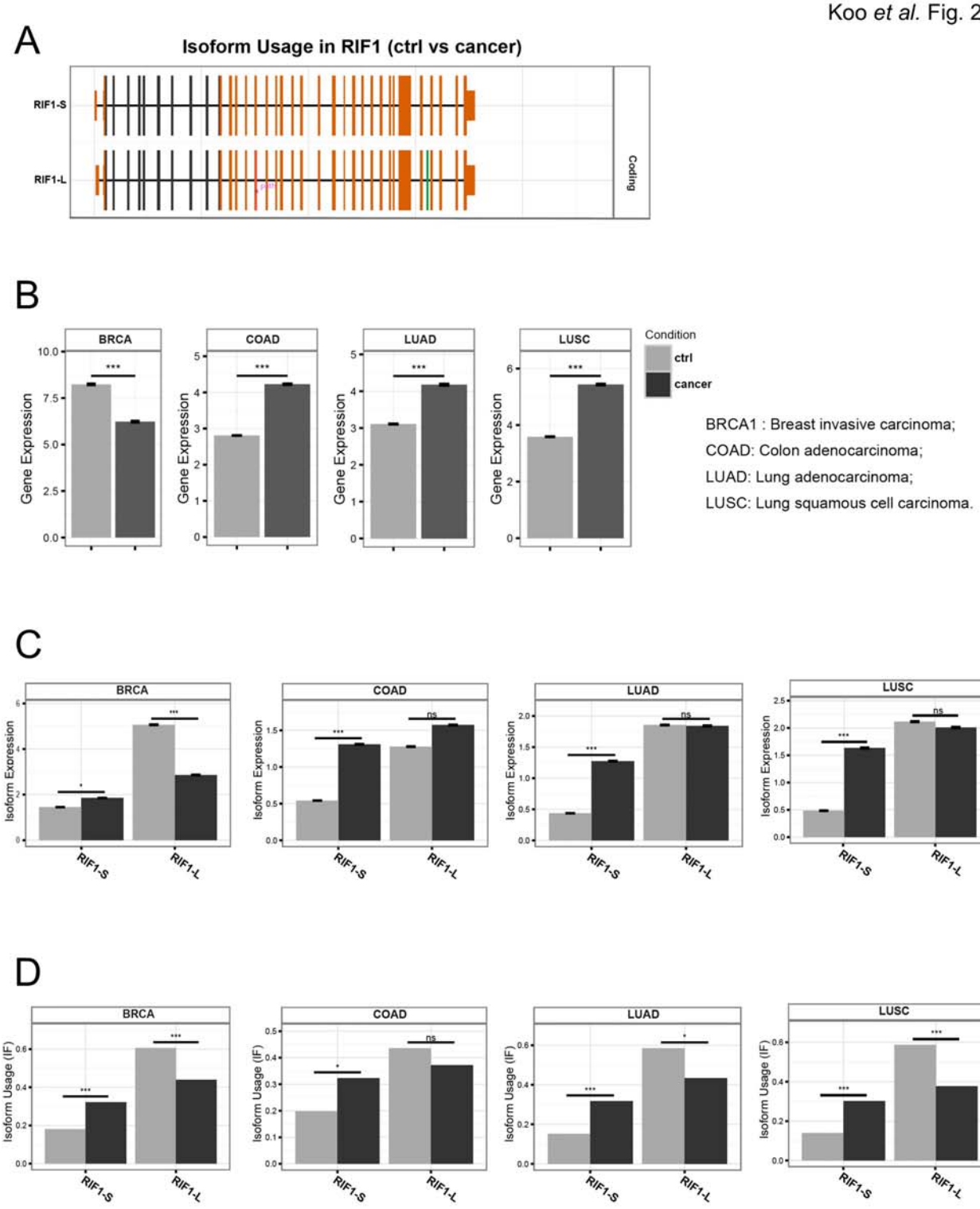

Point mutations in Ex32 prevent its inclusion into RIF1 mRNA

We used CRISPR/Cas9 to disrupt exon 2 (*RIF1*$^{-/-}$), or Ex32 (*RIF1-L*$^{-/-}$) in U-2 OS cells. We generated two *RIF1*$^{-/-}$ lines (H1 and 2C5); two *RIF1-L*$^{-/-}$ lines (A6 and 2A2) containing frameshift mutations in Ex32 leading to the creation of a premature stop codon and likely encoded for truncated RIF1-L proteins; and a third *RIF1-L*$^{-/-}$ line (H11) harboring a homozygous 15 nt deletion that removes amino acids 2261-2265 (Fig. 3A). Interestingly, all three *RIF1-L*$^{-/-}$ cell lines showed dramatic reductions in RIF1-L transcript and a corresponding increase in RIF1-S transcript while mutations in Ex1a (*RIF1*$^{-/-}$) had no impact on the relative proportion of RIF1-L and RIF1-S transcript (Fig. 3B,C). As expected, RIF1-L protein was undetectable in *RIF1-L*$^{-/-}$ (2A2) U-2 OS cells while total RIF1 levels were only slightly reduced relative to controls (Fig. 3D). On the other hand, *RIF1-L*$^{\Delta 5}$ (H11) harboring an in-frame deletion showed a decrease in both RIF1-L and total RIF1 expression in relative to wild-type U-2 OS cells (Fig. 3D, E).

RIF1-S supports lymphoid development and CSR

We also generated two lines of mice selectively deficient for Rif1-L: a *Rif1*^{iA} line harboring a single A insertion between G6604 and G6605 of the Rif1-L coding sequence and *Rif1*$^{\Delta Ex32}$, which harbors a 129 nt deletion spanning the 3' end of intron 31 and the 5' portion of Ex32 (T6477-G6605) (Fig. 3F). Similar to what was observed in U-2 OS cells harboring point mutations in Ex32, expression of Rif1-L mRNA was greatly reduced in testis extracts prepared from *Rif1*$^{iA/iA}$ mice, while Rif1-S mRNA was correspondingly upregulated, likely owing to a defect in Ex32 splicing (Fig. 3G). The fact that the iA mutation greatly reduced the Rif1-L/Rif1-S mRNA ratio supports the idea that Ex32 contains an exonic splicing enhancer (ESE) that is sensitive to small indels. Residual Rif1-L transcripts in *Rif1*$^{iA/iA}$ animals contain a premature termination codon in Ex32 and are likely substrates for the nonsense mediated mRNA decay (NMD) pathway. As expected, Rif1-L protein was undetectable in homozygous *Rif1*$^{iA/iA}$ mice while Rif1-S protein levels were upregulated relative to *Rif1*$^{+/+}$ mice (Fig. 3H).

Homozygous *Rif1*^{iA} and *Rif1*$^{\Delta Ex32}$ mice were fertile, outwardly normal in appearance, and exhibited normal B and T cell development; normal proportions of mature B and T cells; and comparable rates of mitogen-induced B and T cells proliferation (Sup. Fig. 5A-G). Because null mutations in RIF1 impair CSR [4,7], we measured *in vitro* immunoglobulin (Ig) class switching in purified B cells of *Rif1*$^{+/+}$ and homozygous *Rif1*$^{\Delta Ex32}$ mice. However, in contrast to *Rif1*$^{-/-}$ mice [4,7], *Rif1*$^{\Delta Ex32}$ mice exhibited normal rates of class switching to IgG1, IgG2a, IgG2b, and IgG3 in response to treatment with α-CD40, LPS, and/or IL-4 (Sup. Fig. 6A-D). Because Rif1-S accounts for all *Rif1* gene dosage in *Rif1*$^{\Delta Ex32}$ mice, these findings indicate that Rif1-L is not required for canonical roles of RIF1 in CSR.

Koo *et al.* Fig. 3

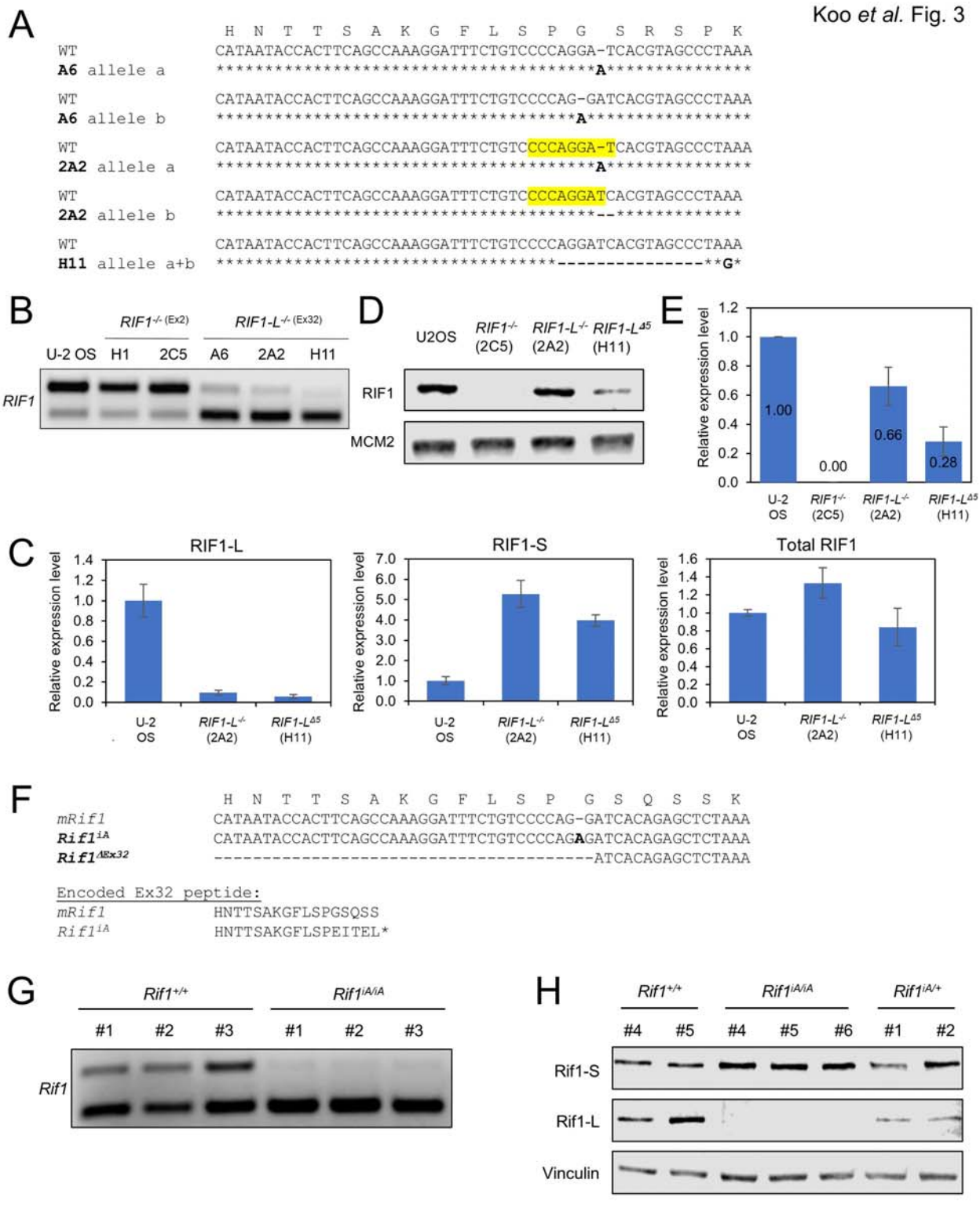

Identification of RIF1 splicing regulators

We carried out a siRNA screen of 151 RNA binding proteins (RBPs) for modulators of RIF1 AS in HeLa cells (Sup Fig. 2A-C) based on the prediction by RBPmap tool (https://doi.org/10.1093/nar/gku406). The primary siRNA screen and secondary shRNA validation screen implicated six RBPs whose silencing changed the RIF1-L/RIF1-S splicing ratio at least two-fold. Polypyrimidine tract-binding protein 1 (PTBP1), RNA Binding Motif Protein 28 (RBM28), serine and arginine-rich splicing factors (SRSFs) 3 and 7 were identified as negative regulators of Ex32 inclusion, whereas small nuclear ribonucleoprotein U1 subunit 70 (snRNP70) and SRSF1 were identified as positive regulators of Ex32 inclusion (Sup. Fig. 2C, Fig. 4A,B). The implication of SRSF1 as a RIF1 splicing factor is consistent with findings of Yu *et al.* who identified RIF1-Ex32 in a screen for SRSF1-regulated splicing events [51]. We included SRSF2 as an additional putative regulator given that its binding site closely overlaps that of SRSF1 [52], and these two splicing factors often work in the same complex with snRNP70 [53]. None of the identified RIF1-Ex32 splicing regulators significantly modulated RIF1-Ex1a splicing in the siRNA screen (not shown).

We next employed native RNA-IP to test whether candidate RIF1 splicing factors directly associated with RIF1 pre-mRNAs. HeLa cell extracts were immunoprecipitated with antibodies specific for SRSF3, SRSF7, PTBP1, SRSF1, SRSF2 and/or snRNP70 or the corresponding normal mouse and rabbit IgG controls. Following elution and purification, bound pre-mRNA was analyzed by RT-qPCR using two different intron-exon primer pairs (Fig. 4C). While there was little to no enrichment of RIF1-Ex32 containing pre-mRNA from snRNP70-IPs, RNA-IP of all other splicing factors showed significant enrichment over IgG IP controls. In addition, both SRSF1 antibodies used (SRSF1-M and SRSF1-R) showed consistent and significant enrichment, strongly implicating SRSF1 as a direct Ex32 binding factor (Fig. 4D,E).

We noted that mutations that disrupted Ex32 inclusion into RIF1 mRNA transcripts in 2A2 and A6 U-2 OS cells were adjacent to a putative SRSF1 binding site (CCCAGGAT) [52-56]. Considering this, we compared SRSF1 binding to RIF1 pre-mRNA between *RIF1*$^{+/+}$ and *RIF1-L*$^{-/-}$ (Clone 2A2) U-2 OS cells. SRSF1 enrichment was not observed in 2A2 U-2 OS cells, suggesting that SRSF1 associates with Ex32 directly through the CCCAGGAT element (Fig. 3A,4F).

RIF1 isoforms behave similarly in DNA replication control

To facilitate study of RIF1-L and RIF1-S isoforms, we reconstituted *RIF1*$^{-/-}$ U-2 OS cells with Dox-inducible, GFP-tagged, RIF1-L and RIF1-S cDNAs (see Materials and Methods) (Sup. Fig. 3A). Both *RIF1*$^{-/-}$:GFP-RIF1-L and *RIF1*$^{-/-}$:GFP-RIF1-S were targeted to IR-induced foci with qualitatively similar magnitude (Sup. Fig. 3B). GFP-RIF1-L and GFP-RIF1-S comparably suppressed MCM4 hyperphosphorylation, which is reflective of unscheduled replication origin firing [47] (Sup. Fig. 3C) and rescued the DNA replication patterning defect seen in *RIF1*$^{-/-}$ cells. Specifically, RIF1-L and RIF1-S restored the perinuclear and perinucleolar EdU incorporation patterns typical of mid-S phase cells that are almost completely absent in *RIF1*$^{-/-}$ cells (Sup. Fig. 4A-C) [57]. Given the basic nature of the S/K cassette and its proximity to the RIF1 DNA binding domain, we measured DNA binding affinity of purified RIF1-L and RIF1-S C-terminal domains (RIF1^{CTD}-L and RIF1^{CTD}-S) by fluorescence anisotropy. Binding of RIF1^{CTD}-L and RIF1^{CTD}-S to an antiparallel G4 substrate was indistinguishable (Sup. Fig. 3D). Hence, we conclude that these canonical measurements of RIF1 function are not significantly impacted by the S/K cassette.

Koo *et al.* Fig. 4

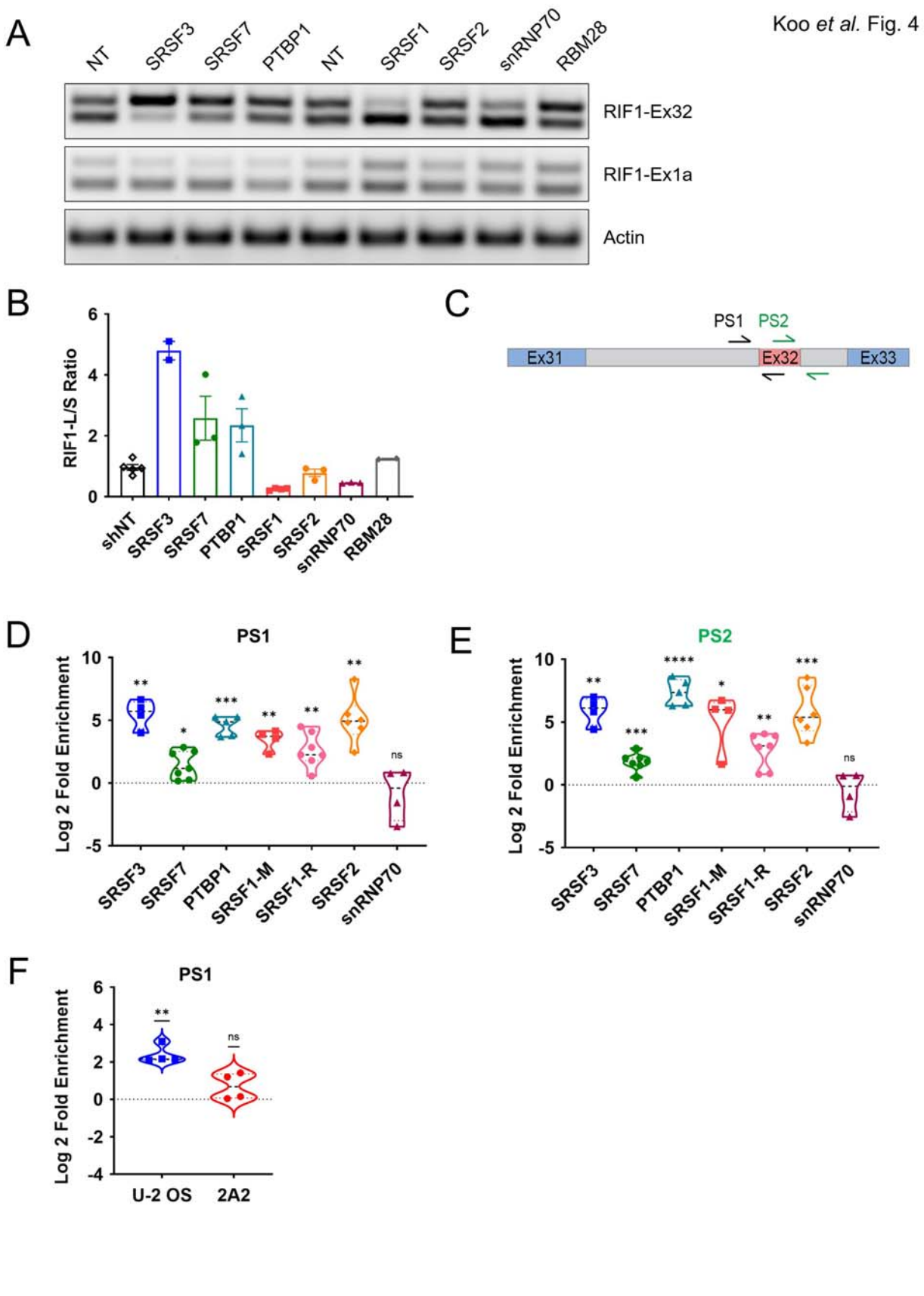

Chromatin proteomic analysis of RIF1 isoforms

We carried out quantitative proteomic analysis of GFP-RIF1-L and GFP-RIF1-S stably expressed in *RIF1*$^{-/-}$ U-2 OS cells. Because relevant RIF1 interactions are likely to occur in the context of chromatin, we adapted the crosslinking-based RIME (rapid immunoprecipitation mass spectrometry of endogenous proteins) in conjunction with label-free quantitative LC-MS/MS [34] (Fig. 5A). We combined data from two technical replicates of three independent RIME crosslinking experiments to identify proteins significantly enriched in α-GFP-RIF1-L and/or α-GFP-RIF1-S immunoprecipitates (IPs) versus α-GFP IPs (Sup. Table 2). Using an FDR of <.05, 451 proteins were significantly enriched in GFP-RIF1-L. A total of 293 proteins were identified in GFP-RIF1-S IPs, of which, 248 were also identified for GFP-RIF1-L (Fig. 5B). The reduced number of interactants for GFP-RIF1-S may reflect reduced chromatin association (see below) or its slightly lower expression in *RIF1*$^{-/-}$ U-2 OS cells (Sup. Fig. 3A).

The dataset of shared RIF1-interacting proteins contained known RIF1 interactors, including PP1, TLK2, ASF1, and 53BP1 [58-61] (Fig. 5C) as well as factors not previously reported to associate with RIF1. Outside of RIF1 itself, the most highly enriched protein in RIF1-L and RIF1-S IPs was Claspin, an adaptor protein that facilitates ATR-dependent activation of the effector kinase CHK1 in response to DNA replication inhibition [62,63]. Other novel RIF1-associated proteins identified in both RIF1-S and RIF1-L IPs include TLK2, a protein kinase implicated in nucleosome assembly, DNA replication and DNA repair; TOP2A, and several proteins involved in mitosis, including TPX2, KIF4A, KIF23, and CENPF [64-68]; the histone chaperone ANP32E [69]; the telomerase-associated pescadillo ribosomal biogenesis factor 1 (PES1); [70] and the mitotic checkpoint regulator CDC20 [71,72] (Fig. 5C,E). Metascape analysis identified DNA metabolic process, chromatin organization, cell cycle, DNA replication, and DNA repair as overrepresented gene functional groups in RIF1-L/S chromatin proteomes (Fig. 5D).

A comparison of the GFP-RIF1-L and GFP-RIF1-S RIME datasets yielded a total of 94 differentially enriched proteins (Fig. 5B); however, 64 of these were excluded from further analysis because they were not significantly enriched in either GFP-RIF1-L or GFP-RIF1-S IPs relative to GFP controls. Of the remaining 30 proteins, 11 were detected in both GFP-RIF1-L and GFP-RIF1-S, but were more enriched in GFP-RIF1-L; 18 proteins were selectively enriched in GFP-RIF1-L IPs; and 1 protein, the NHEJ regulator PAXX [73], was selectively enriched in GFP-RIF1-S IPs (Fig. 5E).

The two proteins showing the greatest fold-change difference between GFP-RIF1-L and GFP-RIF1-S IPs were the nuclear import receptor karyopherin A 3 (KPNA3) and mediator of DNA damage checkpoint 1 (MDC1) (Fig. 5E, Sup. Table 2). The apparent ~4-fold enrichment of MDC1 in RIF1-L IPs is consistent with a study by Gupta *et al.* that identified RIF1 peptides in MDC1 proximity labeling studies [9], and was particularly interesting given that MDC1 recruits RNF8 and consequently 53BP1 and RIF1 to the sites of DNA damage [5,65-67,74-76]. While we could not establish co-immunoprecipitation between MDC1 and RIF1 by Western blotting, a proximity ligation assay (PLA) revealed that endogenous MDC1 was associated with both RIF1-L and RIF1-S (Fig. 5F). In support of the enhanced interaction between MDC1 and RIF1-L seen in the RIME-MS analysis, the number of PLA foci was greater in GFP-RIF1-L U-2 OS versus GFP-RIF1-S U-2 OS cells, and this interaction was further strengthened upon irradiation (Fig. 5F).

Given these findings, we evaluated IR-induced MDC1 focus formation in *RIF1*$^{+/+}$, *RIF1*$^{-/-}$, GFP-RIF1-L, and GFP-RIF1-S U-2 OS cells. The number of MDC1 foci was significantly reduced *in RIF1*$^{-/-}$ cells relative to *RIF1*$^{+/+}$ cells 3 h after exposure to IR, suggesting RIF1 enhances stable MDC1 recruitment (Fig. 5G). Furthermore, MDC1 foci were more abundant in GFP-RIF1-L U-2

OS cells versus GFP-RIF1-S U-2 OS cells, suggesting that RIF1-L amplifies MDC1 accumulation at DSBs.

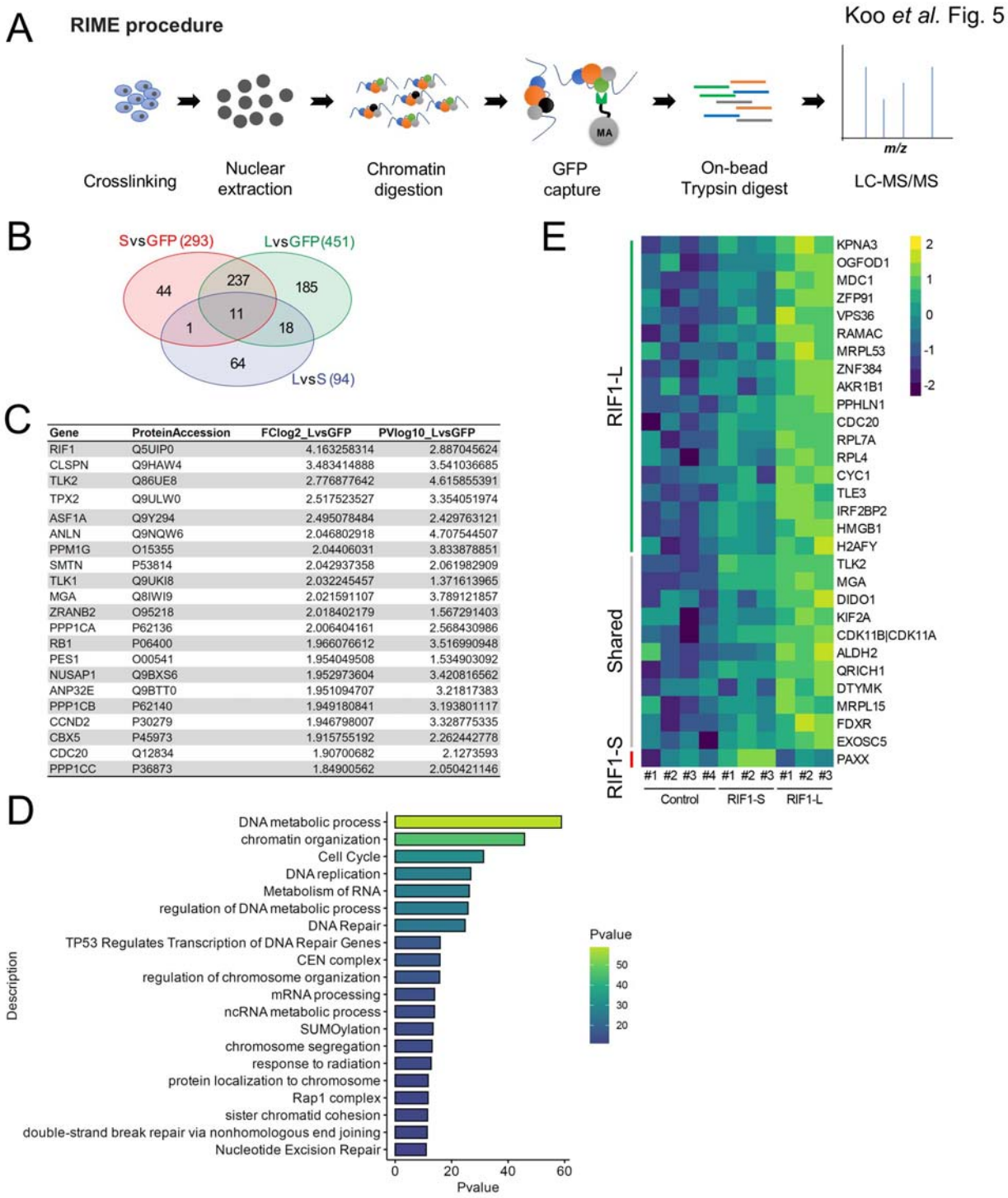

Gene	ProteinAccession	FClog2_LvsGFP	PVlog10_LvsGFP
RIF1	Q5UIP0	4.163258314	2.887045624
CLSPN	Q9HAW4	3.483414888	3.541036685
TLK2	Q86UE8	2.776877642	4.615855391
TPX2	Q9ULW0	2.517523527	3.354051974
ASF1A	Q9Y294	2.495078484	2.429763121
ANLN	Q9NQW6	2.046802918	4.707544507
PPM1G	O15355	2.04406031	3.833878851
SMTN	P53814	2.042937358	2.061982909
TLK1	Q9UKI8	2.032245457	1.371613965
MGA	Q8IWI9	2.021591107	3.789121857
ZRANB2	O95218	2.018402179	1.567291403
PPP1CA	P62136	2.006404161	2.568430986
RB1	P06400	1.966076612	3.516990948
PES1	O00541	1.954049508	1.534903092
NUSAP1	Q9BXS6	1.952973604	3.420816562
ANP32E	Q9BTT0	1.951094707	3.21817383
PPP1CB	P62140	1.949180841	3.193801117
CCND2	P30279	1.946798007	3.328775335
CBX5	P45973	1.915755192	2.262442778
CDC20	Q12834	1.90700682	2.1273593
PPP1CC	P36873	1.84900562	2.050421146

Koo *et al.* Fig. 5, *cont.*

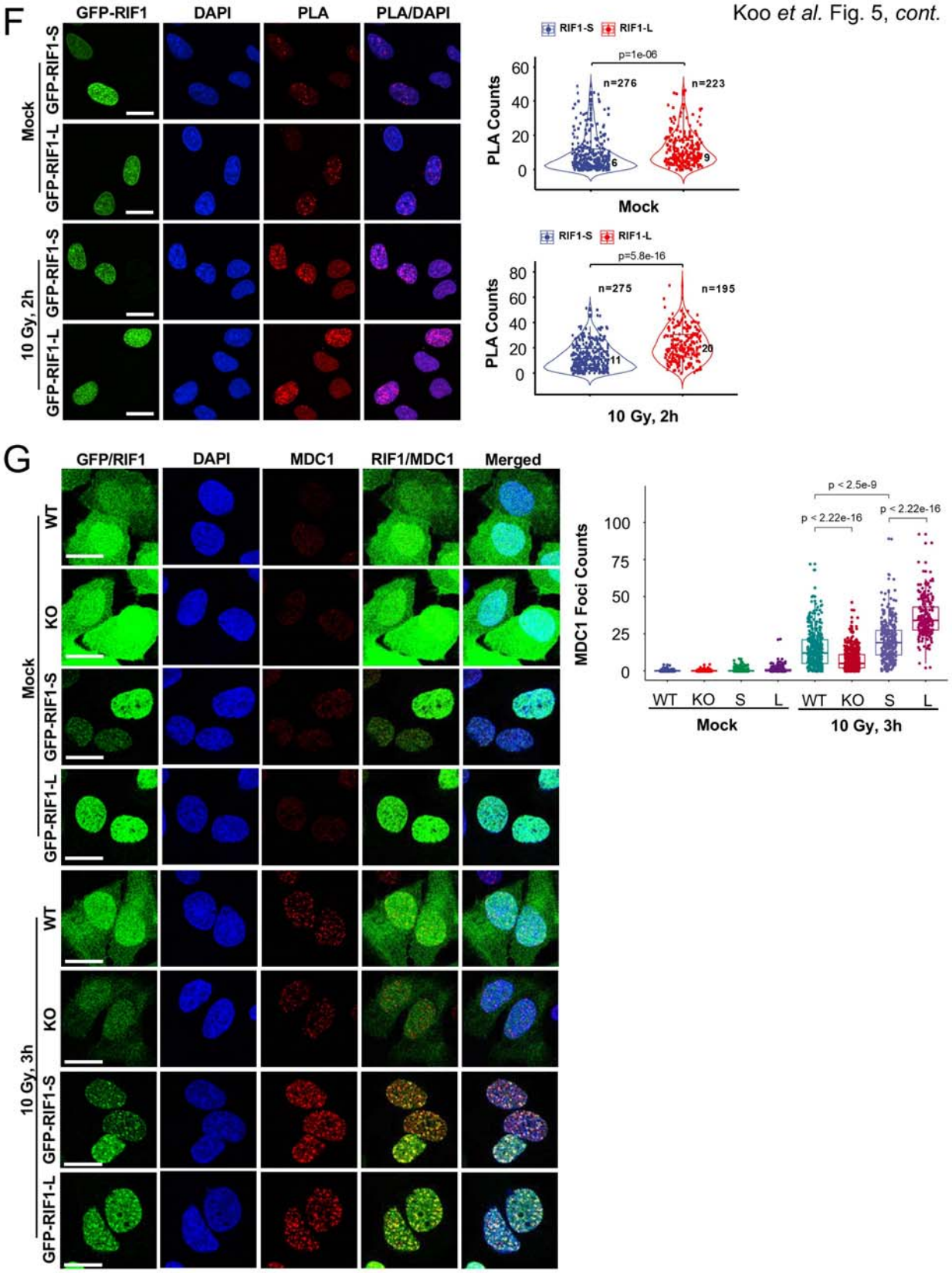

CTD phosphorylation diminishes RIF1 chromatin association

Orbitrap MS identified several phosphorylation sites in GFP-RIF1^{CTD}-L, including S2205, which is located in the PP1 binding site; S2260 and S2265, which are located in Ex32-encoded S/K cassette (Fig. 6A); and S2348, which lies within CR2. We generated phospho-specific antibodies against a peptide dually phosphorylated on S2260 and S2265 (α-RIF1-pS2260/65) and validated the site-specificity of the antibody in Western blotting experiments using GFP-RIF1-L^{1A} and GFP-RIF1-L^{2A} mutants with Ala mutation at site(s) S2260 and S2260/65. GFP-RIF1-L^{1A} reduced α-RIF1-pS2260/65 recognition dramatically while GFP-RIF1-L^{2A} completely abolished recognition by this antibody (Fig. 6B). Using Nocodazole-synchronized U-2 OS cells, we found that RIF1-pS2260/65 phosphorylation was maximal in mitosis and rapidly extinguished following mitotic exit (Fig. 6C).

Although the kinase(s) responsible for S2260 and S2265 phosphorylation are not known, both Ser residues occur in a Ser-Pro dipeptide motif which is a consensus for the mitotic cyclin-dependent kinase 1 (CDK1) and related kinases. A recent study suggested that, under conditions of ATR inhibition, CDK1-dependent phosphorylation of RIF1 on S2205 diminished PP1 binding, leading to increased phosphorylation stoichiometry of CDK2 and CDC7 substrates and elevated rates of origin firing [77,78]. To determine whether S2260 and S2265 phosphorylation exhibit a similar phosphorylation profile, we measured RIF1-pS2260/65 levels in GFP-RIF1-L U-2 OS cells cultured in the presence of a Wee1 inhibitor (AZD1775) or an ATR inhibitor (AZD6738). AZD1775 treatment significantly increased RIF1-pS2260/65 level 1 h after treatment, while ATR inhibitors had little effect (Fig. 6D). Thus, RIF1-S2205 and RIF1-S2260/65 phosphorylation sites are co-phosphorylated under conditions of aberrant CDK1 activation.

The basic nature of the S/K cassette suggested it may play a role in nuclear localization, DNA binding, and/or chromatin association. While RIF1-L and RIF1-S exhibited comparable nuclear localization and binding to G-quadraplex DNA substrates (Sup. Fig. 3B, E), chromatin fractionation of full-length GFP-RIF1-L and GFP-RIF1-S suggested that RIF1-L has significantly higher chromatin binding affinity relative to RIF1-S (Fig. 6E, blue bars). Wee1 inhibition using AZD1775 increased the proportion of S2260/65-phosphorylated RIF1-L (RIF1-pS2260/65) and decreased the chromatin association of both RIF1-L and RIF1-S (Fig. 6E, red bars).

To further explore the relationship between RIF1 phosphorylation and its chromatin association, we compared the chromatin association profiles of GFP-RIF1^{CTD}-L^{WT} to that of GFP-RIF1^{CTD}-L^{7SA}, and GFP-RIF1^{CTD}-L^{7SD} mutants harboring seven Ser-Ala (SA) or Ser-Asp (SD) mutations at UniProt-annotated CDK1 phosphorylation sites, including S2260 and S2265, within the S/K cassette (Fig. 6A). Similar to what was observed using full-length RIF1-L, the phosphorylation of RIF1^{CTD}-L^{WT} on S2260/65 was significantly increased in response to WEE1 inhibition with AZD1775 (Fig. 6F, left panel). In addition, the RIF1-pS2260/65 signal was strongly enriched in the soluble fraction (SF) relative to the chromatin fraction (CF), suggesting that phosphorylation reduces RIF1^{CTD} chromatin-binding affinity. Consistent with this, the phosphomimetic RIF1^{CTD}-L^{7SD} mutant exhibited a significant reduction in chromatin association even without AZD1775 treatment (Fig. 6F, center panel and Fig. 6G). While the RIF1^{CTD}-L^{7SA} mutant exhibited lower expression, its chromatin binding profile was similar to RIF1^{CTD}-L^{WT} (Fig. 6F, right panel and Fig. 6G). As expected, Western blotting with RIF1-pS2260/65 antibodies did not yield a signal in U-2 OS cells expressing either RIF1^{CTD}-L^{7SD} or RIF1^{CTD}-L^{7SA}. Altogether, findings with full-length RIF1 and RIF1^{CTD} fragments suggest that multiple phosphorylation sites within the RIF1 CTD, including S2260/2265 in the S/K cassette, diminish RIF1 chromatin binding in response to WEE1 inhibition.

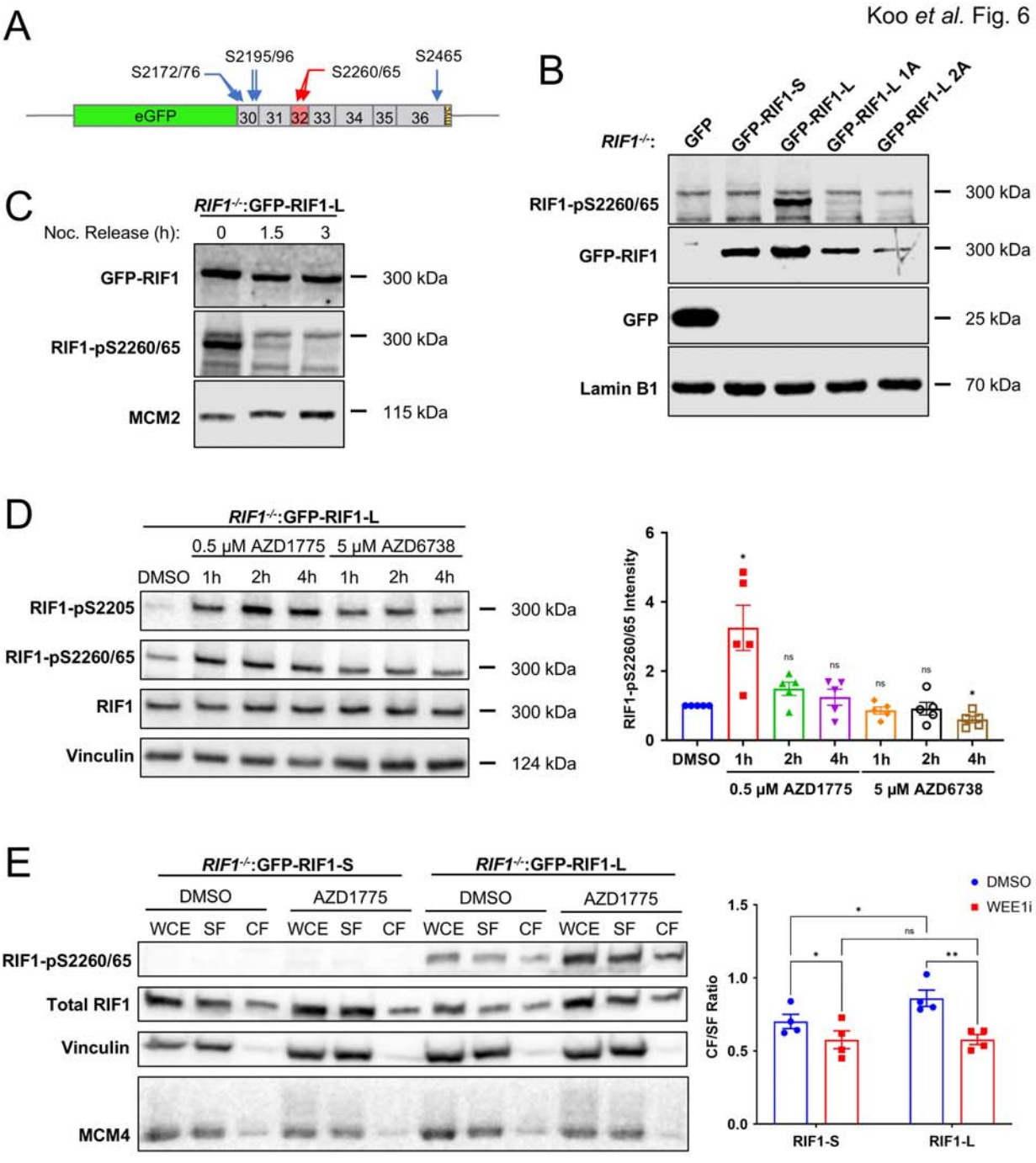

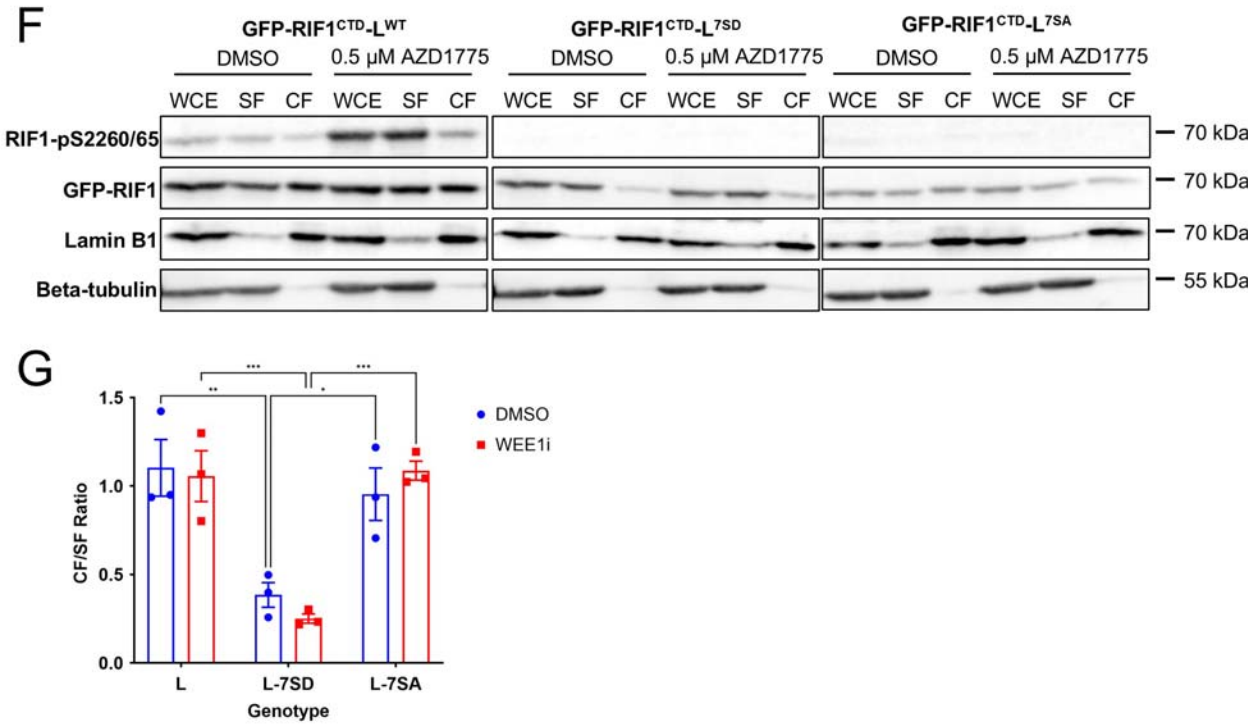

The S/K cassette regulates RIF1 phase separation

Using the DISOPRED 3.1 disorder prediction tool [79], we found that the presence of the S/K cassette reduced disorder of the region roughly spanning amino acids ~2240 to 2280 in the RIF1 CTD (Fig. 7A). In transient transfection assays, GFP-RIF1^{CTD}-L and GFP-RIF1^{CTD}-S formed spherical shells in the nuclei of U-2 OS cells that ranged from single shells to complex arrangements containing multiple chambers (Fig. 7B,C). In contrast, GFP-RIF1^{CTD}-L$^{\Delta NLS}$ with a deletion of the nuclear localization signal (NLS) showed diffused GFP signal in the cytoplasm (Fig. 7B). Three-dimensional reconstruction revealed RIF1 nuclear shells to be oblong spheroids with a hollow central core (Sup. Video 1). Because they closely resembled the birefringent “anisosomes” formed by the nuclear RNA-binding protein TDP-43 [80], we have adopted the anisosome nomenclature to describe RIF1^{CTD} nuclear assemblies.

Time lapse imaging revealed RIF1^{CTD} nuclear anisosomes to be dynamic structures that frequently fused to form larger single- or multi-chamber structures (Fig. 7C, Sup. Video 2). In addition, GFP-RIF1^{CTD} anisosomes underwent spontaneous cycles of closure and reopening (Sup. Video 2). While both GFP-RIF1^{CTD}-S and GFP-RIF1^{CTD}-L formed anisosomes they exhibited different properties. GFP-RIF1^{CTD}-S anisosomes exhibited an increased rate of fusion events versus GFP-RIF1^{CTD}-L anisosomes to form larger structures (Fig. 7B, right panel), while GFP-RIF1^{CTD}-L anisosomes occasionally formed nested structures—rarely observed for GFP-RIF1^{CTD}-S—in which smaller anisosomes were enclosed within a larger assembly (Sup. Video 3). These nested anisosomes may be fusion intermediates and were therefore observed more frequently in the less dynamic GFP-RIF1^{CTD}-L which fused slower (Fig. 7B). RIF1^{CTD} nuclear anisosomes were also observed in transiently transfected HeLa and HEK293T cells as well as U-2 OS cells expressing Dox-inducible GFP-RIF1^{CTD}-S and GFP-RIF1^{CTD}-L (not shown).

To better evaluate the dynamics of RIF1^{CTD} anisosomes, we performed fluorescence recovery after photobleaching (FRAP) experiments in which GFP-RIF1^{CTD}-S and GFP-RIF1^{CTD}-L anisosomes were allowed to recover after photobleaching. Both GFP-RIF1^{CTD}-S and GFP-RIF1^{CTD}-L anisosomes rapidly disintegrated following photobleaching, losing their donut-like character with laser exposure before reassembling over the course of 3 min (Fig. 7G, time course/montage, Sup. Video 4-5). The recovery curve of each bleached anisosome was then plotted from the average fluorescent intensity of the bleached region over time (Fig. 7H,I). GFP-RIF1^{CTD}-S anisosomes showed a small but significantly lower t-half value and a larger mobile fraction estimated from the recovery curves of RIF1^{CTD}-S and RIF1^{CTD}-L anisosomes (Fig. 7J,K). Due to the larger heterogeneity within RIF1^{CTD}-L anisosome population (Fig. 7I) and the difficulty in measuring anisosome morphological recovery based on average fluorescent intensity, we also tabulated the frame numbers in which a bleached anisosome formed either a solid ball intermediate or a fully recovered “donut” (Fig. 7G). The formation of both structures after photobleaching was significantly delayed for GFP-RIF1^{CTD}-L versus GFP-RIF1^{CTD}-S, suggesting that GFP-RIF1^{CTD}-L anisosomes are intrinsically more stable than GFP-RIF1^{CTD}-S anisosomes (Fig. 7L,M). Although the reason for GFP-RIF1^{CTD}-L anisosome recovery heterogeneity is unclear, it is conceivable that the expanded interactome for RIF1^{CTD}-L or posttranslational modification of the S/K cassette influences its phase separation dynamics.

The assembly of GFP-RIF1^{CTD} into organized nuclear structures suggested the CTD undergoes liquid-liquid phase separation (LLPS). To test this, we incubated purified, GST-tagged RIF1^{CTD}-S and RIF1^{CTD}-L with 10% Dextran/PEG. Both GST-RIF1^{CTD}-S and GST-RIF1^{CTD}-L underwent concentration-dependent LLPS, however, RIF1^{CTD}-S formed significantly larger droplets compared to RIF1^{CTD}-L with increasing RIF1^{CTD} concentration (Fig. 7D), possibly reflecting increased rates of droplet fusion seen in transient transfection assays (Fig. 7C). Finally, treatment of cells with 3% w/v 1,6-hexanediol that is known to dissolve LLPS droplet [81] disrupted GFP-RIF1 CTD nuclear anisosomes as expected (Fig. 7E).

To investigate the potential role of phosphorylation in RIF1 CTD phase separation, we transfected U-2 OS cells with GFP-RIF1^{CTD}-L and GFP-RIF1^{CTD}-S CTDs harboring the corresponding 7SA/SD and 5SA/SD mutations (Fig. 6A). In contrast to the well-demarcated anisosomes formed by wild-type GFP-RIF1^{CTD}-S, GFP-RIF1^{CTD}-S^{5SA} formed irregularly shaped anisosomes that typically featured a narrow central cavity and thick outer shell. Loss of anisosomal character was even more pronounced for RIF1^{CTD}-S^{5SD}, which exclusively formed irregular nuclear aggregates (Fig. 7F). While the corresponding GFP-RIF1^{CTD}-L^{7SA} and GFP-RIF1^{CTD}-L^{7SD} mutants also exhibited anisosome morphology defects; the changes were less dramatic than those seen in GFP- RIF1^{CTD}-S^{5SA} and GFP-RIF1^{CTD}-S^{5SD}. This was most pronounced for the SD mutations that completely disrupted GFP-RIF1^{CTD}-S anisosomes but only partially inhibited GFP-RIF1^{CTD}-L anisosome formation. The fact that the presence of S/K cassette reduced the impact of disruptive serine mutations on anisosome formation supports the conclusion that this motif stabilized phase separation of the RIF1 CTD.

Koo *et al.* Fig. 7

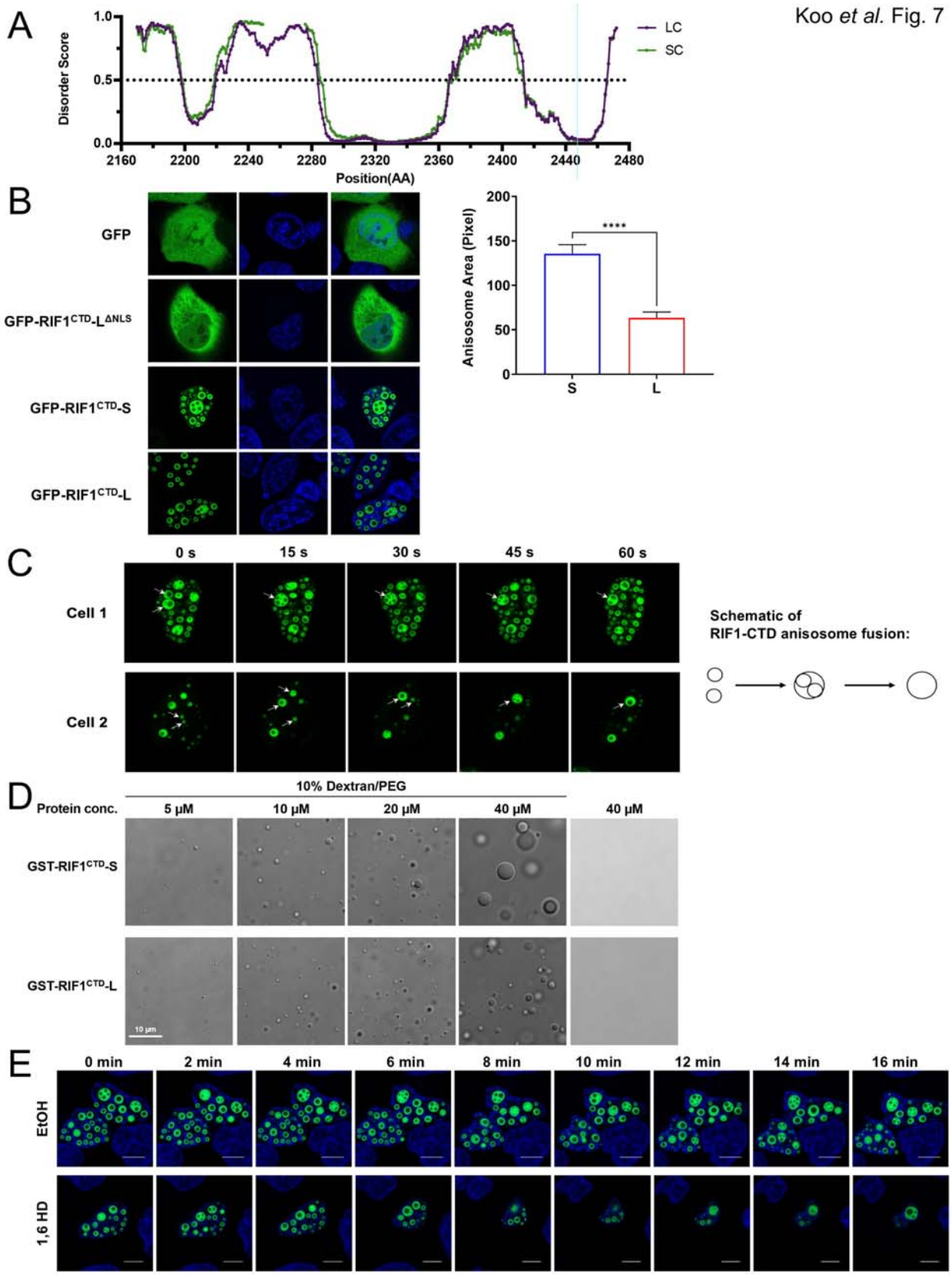

Koo *et al.* Fig. 7, *cont.*

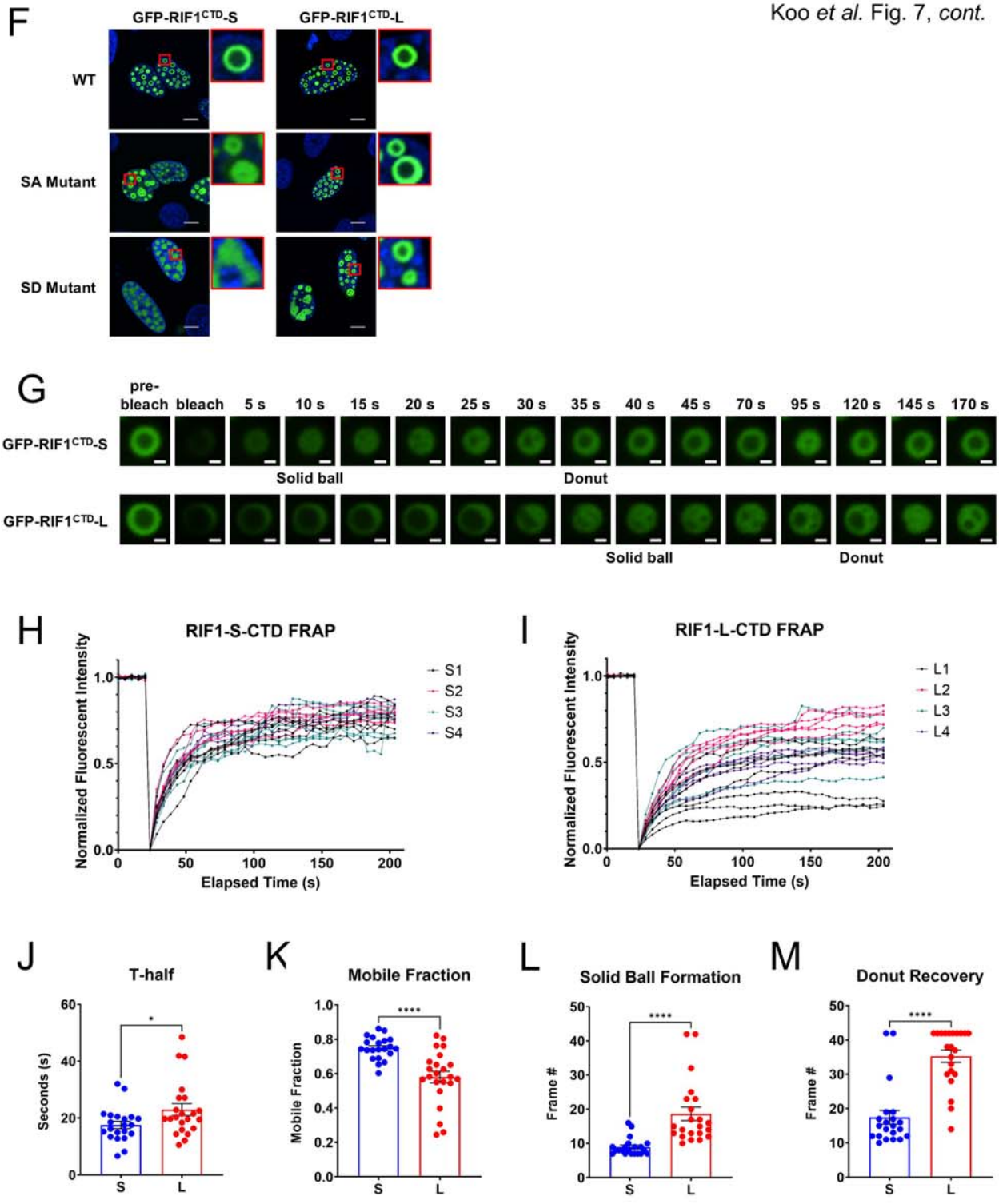

The S/K cassette mediates RIF1-tubulin colocalization

During the course of transient transfection experiments, we occasionally observed that GFP-RIF1^{CTD}-L, but not GFP-RIF1^{CTD}-S, formed ribbon-like structures in the cytoplasm of U-2 OS cells (Sup. Fig. 7B). GFP-RIF1^{CTD}-L ribbons were observed in diverse cell lines; often occurred in the absence of a strong nuclear RIF1 signal and were more likely to occur in cells that recently completed mitosis (not shown). GFP-RIF1^{CTD}-L ribbons strongly colocalized with tubulin, indicating that GFP-RIF1^{CTD}-L associates with microtubules (MTs) in transiently transfected cells (Sup. Fig. 7B).

The occurrence of thickened microtubules in GFP-RIF1-L^{CTD} expressing cells was reminiscent of the tubulin bundling activity of nonmotor microtubule binding protein, MAP65/PRC1, whose bipartite binding to tubulin is enhanced by basic residues in a disordered region [82,83]. To determine whether Lys residues contribute to the MT association of RIF1, we compared localization patterns of GFP-RIF1^{CTD}-L^{WT}, GFP-RIF1^{CTD}-L^{5KQ} and GFP-RIF1^{CTD}-L^{5KR} mutants harboring Gln and Arg mutations at all five Lys residues within the S/K cassette respectively (Sup. Fig. 7A). While GFP-RIF1^{CTD}-L^{5KR} mutants still formed ribbon-like MTs, GFP-RIF1^{CTD}-L^{5KQ} with lysine acetylation mimicking mutations failed to colocalize with MTs, suggesting that the basic residues are essential for tubulin association (Sup. Fig. 7B). By contrast, mutation of two conserved Phe residues to Leu (GFP-RIF1^{CTD}-L^{2FL}) had no effect on RIF1^{CTD}-L MT colocalization (Sup. Fig. 7B).

Next, we investigated contributions of a downstream K/R-rich motif in CR2 for impacts on RIF1-L/MT colocalization (Sup. Fig. 7A, right inset). Interestingly, Lys to Gln mutations in the CR2 K/R motif (GFP-RIF1^{CTD}-L^{4KQ}) was also sufficient to eliminate MT colocalization (Sup. Fig. 7A,B), suggesting the interaction between RIF1 and MTs is bipartite. Finally, we investigated colocalization of an N-terminally truncated GFP-RIF1^{CTD}-L$^{\Delta NLS}$ construct that lacks basic amino acids specifying RIF1 nuclear localization (Sup. Fig. 7A). GFP-RIF1^{CTD}-L$^{\Delta NLS}$ was enriched in the cytoplasm, where it strongly colocalized with MTs. By contrast, the corresponding GFP-RIF1^{CTD}-L$^{\Delta NLS\text{-}5KQ}$ mutant did not associate with MTs and instead formed cytosolic aggregates (Sup. Fig. 7B). We also investigated whether full-length GFP-RIF1 isoforms colocalized with MTs. GFP-RIF1-L, but not GFP-RIF1-S, colocalized with MTs in perinuclear regions of Dox-induced U-2 OS cells (Sup. Fig. 7C). In contrast to findings with the RIF1-L CTD fragment, association between full-length RIF1-L and MTs required prior exposure to DNA damage. While the reason for this discrepancy is unclear, DNA damage may liberate a pool of RIF1 from chromatin. Altogether, these findings indicate that RIF1-L associates with cytosolic tubulin via a bipartite interaction involving basic amino acids in the S/K cassette and CR2.

DISCUSSION

In this study we investigated the mechanisms of RIF1 AS and the functional differences between RIF1-L and RIF1-S isoforms. Our findings suggest that RIF1-L and RIF1-S are functionally interchangeable across most canonical assays of RIF1 function, but possess discernible differences in chromatin association, LLPS, protein interaction network, and tubulin association that likely fine tune RIF1 activity in different physiologic contexts.

The relative abundance between RIF1 isoforms varied across immortalized human cell lines and mouse tissues, with RIF1-L being the predominant species in most instances. Interestingly, while all vertebrate RIF1 orthologs contain an S/K-cassette-like motif in their CTD, alternative splicing in this region is restricted to mammals, indicating that expression of RIF1-S is a recent evolutionary adaptation.

The AS of RIF1 Ex32 in mammalian cells is regulated by no less than six RBPs, including two positive regulators (SRSF1 and snRNP70) and four negative regulators (PTBP1, SRSF3, SRSF7, and RBM28). A central role for SRSF1 as a positive regulator of Ex32 inclusion was supported by its association with RIF1-L mRNA, which was reduced in RIF1^{iA} cells that harbor a mutation in the CCCAGGAT SRSF1 recognition motif (Fig. 4F). Ex32 was also identified as an SRSF1-regulated cassette exon in developing mouse epithelia by Yu *et al.* [84]. Although snRP70 binding was not detected using available antibodies, it is often found within the same alternative splicing complex as SRSF1 where it enhances recognition of the 5' splice site [84,85]. Thus, cooperative activities of SRSF1 and snRNP70 may promote RIF1 Ex32 inclusion in actively dividing progenitor cells and S/G_2-phase cells where RIF1-L levels are high (Fig. 1I,J). By contrast, independent or cooperative binding of SRSF3, SRSF7 and PTBP1 within Ex32 and/or flanking introns (Fig. 4D,E) promotes Ex32 exclusion under conditions of DNA damage and in some primary tumors (Fig. 1E-H, 2C). Although the relative contributions, interrelationships, and binding sites for these inhibitory RBPs remain to be determined, the 3' end of intron 31 in RIF1 contains a conserved pyrimidine-rich tract (TTTTTTTCTCTCCTTTCTTCT) that may mediate PTBP1 binding. Altogether, we propose that levels of Ex32 inclusion are determined by the competitive balance between positive (e.g. SRSF1 and SRSF2) and negative (SRSF3, SRSF7, PTBP1, and RBM28) regulators and that changes in the expression, localization, or activity of these RBPs leads to different rates of Ex32 inclusion under different cellular conditions. We note that SRSF1 was upregulated in osteosarcoma cell lines, such as U-2 OS [86] that expresses high levels of RIF1-L (Fig. 1C), while negative regulators SRSF3, SRSF7, and PTBP1, are pro-oncogenic, anti-apoptotic, and often overexpressed in primary cancers [84,85]. Future studies will investigate the contributions of individual RBPs to RIF1 AS regulation during genotoxic stress and in BRCA, COAD, LUAD, and LUSC (Fig. 2C) associated with low RIF1-L/S splicing ratios.

While the cellular implications of RIF1 AS remain to be fully elucidated, our findings suggest that the Ex32-encoded S/K cassette significantly alters the biochemical properties of the RIF1 CTD leading to enhanced chromatin association, an altered protein-interaction profile, enhanced propensity to undergo LLPS, and novel association with MTs. The basic S/K cassette strengthened the chromatin binding of RIF1-L which was diminished through multisite phosphorylation of the CTD—including at least two sites within the S/K cassette—in response to Wee1 inhibition (Fig. 6D-F). Previous work showed that Wee1 inhibitors induced CDK1-dependent phosphorylation of RIF1 on S2205, leading to PP1 dissociation, MCM4 hyperphosphorylation, and activation of dormant replication origins [77]. We speculate that coregulated PP1 dissociation and chromatin eviction of RIF1 contributes to replication checkpoint failure in response to Wee1 inhibition and CDK1 activation.

RIF1 chromatin proteomics identified both known and novel RIF1 interactants, including the replication factor Claspin, which is of interest owing to its participation in CHK1 activation and replication origin suppression during genotoxic stress [63]. Our MS and PLA findings further suggest that MDC1 interaction is enhanced for the RIF1-L isoform (Fig. 5E,F). Because MDC1 is also a chromatin-associated protein [87], its increased abundance in RIF1-L IPs could be due to the enhanced chromatin association of RIF1-L versus RIF1-S. Alternatively, the S/K cassette could mediate an interaction with MDC1. While the functional significance of the enhanced RIF1-L-MDC1 interaction is presently unclear, our findings suggest that RIF1-L amplifies MDC1 accumulation at sites of DNA damage (Fig. 5G). Further experiments are needed to establish mechanisms and functional consequences of the RIF1-MDC1 interaction.

One protein showed enhanced interaction with RIF1-S under the statistical thresholds employed: the auxiliary NHEJ factor, PAXX. The association of RIF1-S with PAXX suggests the intriguing

possibility that, in addition to its roles in suppressing HDR, RIF1 may also contribute an isoform-specific role in NHEJ (Fig. 5E). Although the precise nature of the RIF1-S-PAXX interaction awaits further study, we note that RIF1-S mRNA is most abundant in G_1 phase when NHEJ is the predominant DSBR pathway (Fig. 1I,J).

The RIF1 CTD undergoes LLPS *in vitro* and forms phase separated, anisosome-like, structures in intact cells [80] (Fig. 7B). While both GFP-RIF1^{CTD}-S and GFP-RIF1^{CTD}-L formed anisosomes, they exhibited distinct characteristics. GFP-RIF1^{CTD}-S anisosomes were larger, more dynamic, fusion prone (Fig. 7C), and exhibited faster FRAP recovery times with larger mobile fraction as a more homogenous species compared to GFP-RIF1^{CTD}-L anisosomes (Fig. 7H-M). Enriched with Arg and Ser, which can function as spacer and sticker respectively to promote phase separation and hardening of the droplet [88], the presence of S/K cassette decreased the molecular dynamics of GFP-RIF1^{CTD}-L and stabilized anisosome structures so that they were less susceptible to disruption by phosphomimetic amino acid substitutions. While full-length RIF1 also formed nuclear structures that may be attributed to phase-separation (not shown), it did not form discrete anisosomes, which may require supraphysiologic levels of RIF1 or may be suppressed by intramolecular folding. Nevertheless, stabilization of RIF1 LLPS by the S/K cassette may contribute to RIF1-dependent replication timing, potentiation of MDC1 accumulation at IR-induced foci, 53BP1 nuclear body formation [28], and other chromatin-associated roles.

An unexpected finding from this study was that RIF1-L selectively associates with MTs in interphase cells (Sup. Fig. 7B,C). While the enhanced association of RIF1^{CTD}-L with MTs may be due to nuclear disruption during apoptosis initiation [89], full-length GFP-RIF1-L also colocalized with MTs in interphase cells that maintained normal cellular morphology with IR exposure (Sup. Fig. 7C). Association with MTs required two basic regions in RIF1-L: the Lys cluster in the S/K cassette and another cluster of Lys residues in a basic patch of CR2. Basic regions have been broadly implicated as MT-binding motifs through interaction with acidic surface patches on β-tubulin [82,90,91]. While the functional implications of MT association are still unclear, multiple mitotic regulators were identified in the RIF1-L/S chromatin proteomes (Fig. 5C-D). In addition, an earlier study reported that RIF1 localizes in proximity to midzone MTs in anaphase [92]. Finally, MTs are instrumental regulators of nuclear shape and have been implicated in the mobilization of damaged chromatin toward repair complexes [93]. Either or both these functions of MTs could be influenced through interactions with RIF1. Understanding the mechanism of selective RIF1-L association with MTs and its functional importance in mitosis, nuclear organization, DNA repair, and other MT-dependent cellular processes awaits further investigation.

CONCLUSION

Our study revealed how DNA damage, cell cycle signaling, and oncogenesis contribute to RIF1 isoform switch through a suite of RBPs and examined several key differences of RIF1 isoform functions. We have linked RIF1-S isoform with a weaker chromatin association to be the dominant isoform expressed in the G_1 phase of the cell cycle, accumulated following DNA damage probably through a reduced expression/activity of the negative splicing regulators such as SRSF3 and SRSF7. RIF1-S preferentially interacts with PAXX in the NHEJ pathway to promote DSBR and cell proliferation—properties of cancers. In contrast, the stronger chromatin-bound RIF1-L isoform favorably interacts with checkpoint proteins such as MDC1 and is expressed maximally in G_2/M phase. RIF1-L might participate in cell cycle checkpoint surveillance through SRSF1 regulation. CDK1 phosphorylation of RIF1 CTD removes S/K-

cassette-specific interactome and eliminates the isoform differences in chromatin binding. The presence of the S/K cassette also completes a bipartite microtubule binding motif which allows only RIF1-L to bind to MTs.

ACKNOWLEDGMENTS

The authors would like to thank Lance A. Rodenkirch (University of Wisconsin Optical Image Facility) for assistance with FRAP experiments and anything microscopy. ASHK thanks Adrian Tan (National Parks Board Singapore) for his biostatistical inputs and all the contributing users on image.sc forum for image analysis inputs. The work was supported by a pilot award from the University of Wisconsin Head and Neck Specialized Program of Excellence (SPORE) to RST and the following grants: 1RF1AG069483-01A1 and 1R01CA180765-01 to RST; AI079087 and HL130724 to DW; R35GM126914 to LMS, MS and CEB.

AUTHOR CONTRIBUTIONS

Conceptualization, RST, WYJ, MS, LMS, JLK, LG, CJB;
Methodology, all;
Investigation, Validation, and Formal Analysis, ASHK, WYJ, MS, CEB, YC, DW, AFV, AB;
Software, Data Curation, and Visualization, ASHK, WYJ, MS, CEB, AFV, AB;
Writing – Original Draft, RST, ASHK and WYJ;
Writing – Review & Editing, all;
Supervision, Resources, and Funding Acquisition, RST, LMS, DW, JLK, LG, CJB;

DECLARATION OF INTERESTS

The authors declare no competing interests.

FIGURE LEGENDS

Figure 1. RIF1 undergoes DNA damage and cell cycle dependent AS. (A) RIF1 protein domains. Blue rectangles from left to right correspond to CR1, CR2 and CR3 respectively. Ex32-encoded S/K cassette is highlighted in red with its sequence shown. CDK1 phosphorylation sites (S2260 and S2265) are in bold. (B) RIF1 Ex32 splicing assay with a forward primer targeting Exon 31 (Ex31) and a reverse primer targeting Exon 33 (Ex33). (C) Exposure to the radiomimetic drug Calicheamicin γ1 (CLM) (10 nM for 6h) reduced the RIF1-L/S mRNA ratio in H460, U-2 OS, HEK293T and HeLa cells. (D) Differential response of RIF1 and TRIP12 AS to CLM. U-2 OS cells were treated with 10 nM CLM for 6 h and the total mRNA was analyzed for Ex32 and Ex3 inclusion in RIF1 and TRIP12, respectively. (E) CLM dose dependence of RIF1 splicing regulation in HeLa cells treated with the indicated CLM concentration for 4 h. (F) Time dependence of RIF1 splicing regulation by 10 nM CLM in U-2 OS cells. (G, H) Dose dependence ionizing radiation (IR)-induced repression of Ex32 inclusion in H460 cells 6 h after exposure. The mean RIF1-L/S mRNA ratio and standard error was calculated by densitometry. Each dot represents an individual biological replicate, N = 3. (I, J) RIF1 AS in HeLa cells fluctuates during the cell cycle. HeLa cells were released from a double-thymine block and harvested at the indicated times. The mean RIF1-L/S mRNA ratio and standard error was calculated by densitometry. Each dot represents an individual biological replicate, N = 3.

Figure 2. RIF1 Ex32 splicing changes differently across cancer types. (A) Exonic structure of RIF1-S and RIF1-L. (B-C) RIF1 isoform expression data was estimated from The Cancer Genome Atlas (TCGA) data through IsoformSwitchAnalyzeR (B) Total RIF1 gene expression in breast invasive carcinoma (BRCA) (Control, N = 114; Cancer, N = 1097), colon adenocarcinoma (COAD) (Control, N = 41; Cancer, N = 460), lung adenocarcinoma (LUAD) (Control, N = 59; Cancer, N = 516), and lung squamous cell carcinoma (LUSC) (Control, N = 51; Cancer, N = 502) (***. FDR < 0.001 from EdgeR for expression tests and two-tailed Mann-Whitney test). (C) The proportion of RIF1-S transcript relative to RIF1-L transcript in all four cancer types (ns. not significant; *. FDR < 0.05; ***. FDR < 0.001 from EdgeR for expression tests and two-tailed Mann-Whitney test). (D) RIF1 isoform usage (ns. not significant; *. FDR < 0.05; ***. FDR < 0.001).

Figure 3. Point mutations in Ex32 diminish RIF1-L transcript formation. (A) Three *RIF1-L*$^{-/-}$ U-2 OS clones (A6, 2A2, and H11) harboring CRISPR-induced mutations (in bold) aligned to the wild-type (WT) RIF1-Ex32 allele. A6 and 2A2 have two distinct alleles whereas H11 are homozygous. Disrupted SRSF1 binding site in Clone 2A2 was highlighted in yellow. (B,C) Reduced expression of RIF1-L transcript and a corresponding increase in RIF1-S transcript in *RIF1-L*$^{-/-}$ U-2 OS cell lines. Total RIF1 transcripts stayed relatively constant in WT and mutated U-2 OS cell lines. CRISPR-generated mutations in RIF1-Exon 2 (Ex2) (Clones H1 and 2C5), did not change RIF1-Ex32 AS. (D, E) Western blot analysis showed that *RIF1-L*$^{-/-}$ (Clone 2A2) and *RIF1-L*$^{\Delta 5}$ (Clone H11) have reduced total RIF1 expression while Clone 2C5 (*RIF1*$^{-/-}$) has an undetectable RIF1 expression. (F) Murine *Rif1* alleles generated through CRISPR-mediated gene editing of Ex32. *Rif1*^{iA} mice harbor a single A insertion whereas *Rif1*$^{\Delta Ex32}$ has a 129 nt deletion spanning Intron 31 and Ex32. (G) RIF1 splicing assay (N = 3) showing reduced expression of RIF1-L and increased expression of RIF1-S transcript in testis from homozygous *Rif1*^{iA} mice. (H) Western blot analysis of RIF1-L and RIF1-S protein expression in *Rif1*$^{+/+}$, *Rif1*$^{iA/+}$, and *Rif1*$^{iA/iA}$ testis extracts using isoform-specific antibodies showed a similar trend in (G).

Figure 4. Identification of RBPs that regulate RIF1 AS and associate with RIF1 pre-mRNAs. (A) Lentiviral shRNA vectors targeting putative RIF1 splicing regulators were transduced into HeLa cells to assess effects on Ex32 and Ex1a AS. Non-targeting (NT) shRNA served as a negative control. (B) Quantification of RIF1-L/RIF1-S mRNA ratios from (A) based on densitometry. Bar height corresponds to mean and standard error. $2 \geq N \geq 5$. (C) Relative locations of the two intron-exon primer pairs used in RNA-IP qPCR experiments. PS1 targets RIF1-In31 and Ex32 whereas PS2 targets RIF1-Ex32 and In32. (D, E) Relative log2 fold enrichment from native RNA-IP experiments in HeLa cells with antibodies targeting the indicated RBPs from PS1 and PS2 amplification as indicated in (C). Median and interquartile range were shown as dotted lines, each dot represents an individual biological replicate, $4 \geq N \geq 7$. (F) Relative log2 fold enrichment from native RNA-IP experiments done in WT U-2 OS cells and Clone 2A2 (*RIF1-L*$^{-/-}$ U-2 OS, Fig. 3). N = 4. For each target/antibody, a two-tailed one sample t-test was performed under the null hypothesis that there is no enrichment (ns. not significant; *. $p \leq 0.05$; **. $p \leq 0.01$; ***. $p \leq 0.001$; ****. $p \leq 0.0001$).

Figure 5. Chromatin proteomic analysis of RIF1 isoforms showed isoform-specific interactome. (A) Flow chart of the RIF1 RIME procedure. (B) Venn diagram showing proteins significantly enriched in GFP-RIF1-S (red) and GFP-RIF1-L (green) IPs (relative to GFP controls) and proteins differentially enriched between GFP-RIF1-S and GFP-RIF1-L IPs (blue). (C) Top 20 enriched proteins common to GFP-RIF1-S and GFP-RIF1-L datasets. (D) Metascape pathway analysis of the shared GFP-RIF1-L/S interactome. (E) Heat map representation of 30 proteins showing differentially enriched proteins shared between GFP-RIF1-L and GFP-RIF1-S IPs. (F) The interaction between MDC1 and RIF1 isoforms was evaluated by PLA using GFP, GFP-RIF1-S, and GFP-RIF1-L U-2 OS cells. Cells were processed for PLA using GFP (Santa Cruz sc9996, 1:250) and MDC1 (Sigma HPA006915, 1:500) antibodies 2 h after exposure to 10 Gy IR or without IR (Mock). The total number of cells analyzed (n), the median number of PLA foci per condition, and the p-value from Wilcox test were shown inside the violin plots. Each dot represents the PLA count number from an individual cell. Scale bar = 20 μm. (G) RIF1-L enhanced MDC1 foci formation. *RIF1*$^{+/+}$, *RIF1*$^{-/-}$, *RIF1*$^{-/-}$:GFP-RIF1-S, and *RIF1*$^{-/-}$:GFP-RIF1-L U-2 OS cells were mock irradiated or exposed to 10 Gy IR followed by 3 h recovery and then fixed and stained with MDC1 antibodies. Foci analysis was performed on a minimum of 50 cells per genotype. The p-values from Wilcox test were shown in the plot. Each dot represents the number of MDC1 foci from an evaluated cell.

Figure 6. RIF1 phosphorylation on S2260 and S2265 during mitosis and in response to Wee1 inhibitor decreases its chromatin association. (A) Schematic of GFP-RIF1^{CTD}-L construct showing five UniProt-annotated phospho-Ser residues (blue arrows) and S2260/65 (red arrows). These selected Ser residues were subsequently mutated to Asp or Ala. (B) Specificity of α-RIF1-pS2260/65 antisera was tested with lysates from *RIF1*$^{-/-}$ U-2 OS cells expressing GFP or the indicated RIF1 alleles. RIF1-L^{1A} and RIF1-L^{2A} alleles harbor Ala mutations at S2260 and S2260/S2265, respectively. (C) *RIF1*$^{-/-}$:GFP-RIF1-L U-2 OS cells were synchronized in prometaphase with nocodazole (Noc) and released into Noc-free media for the indicated lengths of time. Note rapid reduction in RIF1-pS2260/65 levels following Noc release. (D, left panel) *RIF1*$^{-/-}$:GFP-RIF1-L U-2 OS cells were treated with Wee1 inhibitor (AZD1775) or ATR inhibitor (AZD6738) for the indicated timepoint prior to immunoblotting analysis. Monoclonal RIF1-pS2205 antibody was obtained from Christopher Bakkenist's lab and used at a dilution of 1:1000. (D, right panel) The mean intensity of RIF1-pS2260/65 of each treatment was normalized to the baseline phosphorylation level in DMSO control, standard error was shown. Each dot represents an individual biological replicate, N = 5. A two-tailed one sample t-test was performed (ns. not significant; *. $p \leq 0.05$). (E, left panel). Representative Western blot

showing the chromatin fractionation patterns for GFP-RIF1-L and GFP-RIF1-S in DMSO or 0.5 μM AZD1775 for an hour. Whole-cell (WCE), chromatin (CF), and soluble fraction (SF) were resolved by SDS-PAGE and blotted with the indicated antibodies. (E, right panel) Quantification of the mean chromatin/soluble fraction (CF/SF) ratio of total RIF1-L/RIF1-S, standard error was shown. Each dot represents an individual biological replicate, N = 4. A two-way ANOVA with uncorrected Fisher's LSD test was performed (ns. not significant; *. $p \leq 0.05$; **. $p \leq 0.01$). (F, G) Phosphorylation and chromatin fractionation patterns of GFP-RIF1^{CTD}-L. The indicated GFP-RIF1^{CTD}-L constructs were transiently expressed in U-2 OS cells treated with DMSO or 0.5 AZD1775 for an hour. Note that phospho-GFP-RIF1^{CTD}-L^{WT} and phosphomimetic GFP-RIF1^{CTD}-L^{7SD} were highly enriched in the SF, while GFP-RIF1^{CTD}-L^{7SA} with abolished phosphorylation sites was not. (G) Quantification of the mean CF/SF ratio of GFP-RIF1 in (F) with standard error was shown. Each dot represents an individual biological replicate, N = 3. A two-way ANOVA with Tukey's multiple comparisons test was performed (*. $p \leq 0.05$; **. $p \leq 0.01$; ***. $p \leq 0.001$).

Figure 7. RIF1 CTD undergoes LLPS where RIF1^{CTD}-S anisosomes have higher disorder and are more dynamic than RIF1^{CTD}-L. (A) Predictive disorder score of GFP-RIF1^{CTD}-S and GFP-RIF1^{CTD}-L showed that the presence of S/K cassette (2250 – 2275 aa) decreases the disorder of RIF1 CTD. (B, left panel) Representative examples of RIF1 CTD nuclear assemblies. U-2 OS cells were transiently transfected with GFP, GFP-RIF1^{CTD}-L$^{\Delta NLS}$, GFP-RIF1^{CTD}-S or GFP-RIF1^{CTD}-L and subjected to live cell imaging. (B, right panel) Quantification of mean anisosome area with standard error. Unpaired two-tailed t-test assuming equal standard deviation was performed. N = 586 for GFP-RIF1^{CTD}-S; N = 396 for GFP-RIF1^{CTD}-L (***. $p \leq 0.0001$). (C) Timelapse images and the schematic showing the fusion of GFP-RIF1^{CTD} anisosomes in 60 seconds. Single anisosomes and the subsequently fused multi-chambers anisosomes were marked with white arrows. (D) *In vitro* phase separation assays showed concentration (10-40 μM) dependent LLPS droplet formation of purified GST-RIF1^{CTD}-S and GST-RIF1^{CTD}-L proteins. Scale bar = 10 μm. (E) GFP-RIF1^{CTD}-S anisosomes in U-2 OS cells disintegrated over the course of 16 min with the treatment of 3% w/v 1,6-hexanediol which disturbed the formation of phase separation droplets. Scale bar = 10 μm. (F) Serine to alanine (SA) and serine to aspartic acid (SD) mutations impede anisosome formation to a greater extent in GFP-RIF1^{CTD}-S expressing cells. Red boxes showed enlargement of the anisosomes of interest. Scale bar = 10 μm. (G) Fluorescence recovery after photobleaching (FRAP) montage for representative GFP-RIF1^{CTD}-S and GFP-RIF1^{CTD}-L anisosomes in U-2 OS cells. Scale bar = 1 μm. (H, I) FRAP recovery curves of the bleached anisosomes for GFP-RIF1^{CTD}-S and GFP-RIF1^{CTD}-L over a time course of three minutes. Four biological replicates were carried out, each with at least three technical replicates. Each recovery curve was color-coded according to the biological replicate number in the plot. (J, K) Each recovery curve from (H) and (I) was fitted by single exponential equation to estimate the t-half value of recovery and mobile fraction of the anisosome. Unpaired two-tailed t-tests with Welch's correction which does not assume equal standard deviation in populations were performed. (L, M) Manual tabulation of the recovery frame where the two distinct stages – "solid ball" and "donut", as indicated in (G) – reappeared after photobleaching was done. Unpaired two-tailed t-tests with Welch's correction were performed (*. $p \leq 0.05$; ****. $p \leq 0.0001$).

SUPPLEMENTARY VIDEOS

https://github.com/adenine-koo/RIF1_Raw-Sup_data

Sup. Video 1. Three-dimensional reconstruction of RIF1^{CTD}-S anisosomes which resembled oblong spheroids from 10x 1 µm image sections taken at ~ 25 s interval for a total of 534 s.

Sup. Video 2. Three-dimensional reconstruction of RIF1^{CTD}-S anisosomes from 7x 2 µm image sections taken at 10.7 s interval for a total of 311 s, showing the dynamics of anisosomes and fusion events.

Sup. Video 3. RIF1^{CTD}-L^{5KQ} (and other RIF1^{CTD}-L variants) formed nested anisosome structures in which at least one smaller anisosome was formed within a bigger anisosome. Acquisition time interval = 1.1 s, scale bar = 10 µm. Note that this is a video from FRAP experiment so there was a bleaching event of 2 s before Frame #3.

Sup. Video 4. FRAP video images of RIF1^{CTD}-S. Red arrow marked the bleached anisosome. Scale bar = 10 µm.

Sup. Video 5. FRAP video images of RIF1^{CTD}-L. Red arrow marked the bleached anisosome. Scale bar = 10 µm.

SUPPLEMENTARY TABLES

https://github.com/adenine-koo/RIF1_Raw-Sup_data

Sup. Table 1. siRNA key for the numbering used in Sup. Fig. 2B.

Sup. Table 2. Sheet 1 showed the results of student t-test performed on each of the 2784 genes between α-GFP-RIF1-L and α-GFP-RIF1-S immunoprecipitates (IPs) with the 94 significantly enriched genes selected and grouped in Sheet 2. Sheets 3 and 4 showed the student t-test results for the 2784 genes for α-GFP-RIF1-L or α-GFP-RIF1-S with α-GFP IP. Sheet 5 showed the results of two-way ANOVA with Tukey's multiple comparisons that were performed on the 378 significantly enriched genes between α-GFP-RIF1-L, α-GFP-RIF1-S and α-GFP IPs.

SUPPLEMENTARY FIGURE LEGENDS

Sup. Fig. 1. Effects of canonical DNA damage repair inhibitors on CLM-dependent RIF1 AS. (A) U-2 OS cells treated with CLM with or without PARP inhibitor for 4 h. The mean RIF1-L/S mRNA ratio and standard error was calculated by densitometry. Each dot represents an individual biological replicate, N = 3. (B) U-2 OS cells treated with CLM, ATM or DNA-PK inhibitor for 4 h. (A-B) The mean RIF1-L/S mRNA ratio and standard error was calculated by densitometry. Each dot represents an individual biological replicate, N = 4.

Sup. Fig. 2. **RNAi screen for RIF1 splicing regulators**. (A) Schematic of RNAi screen in HeLa cells with 151 siRNAs targeting genes for RNA binding proteins and a non-targeting siRNA control. (B) RIF1 splicing in HeLa cells transfected with the indicated siRNAs (see Sup. Table 1 for the numbering key). Green labels denote candidate positive regulators of Ex32 inclusion; red labels denote putative inhibitors of Ex32 inclusion. (C) Candidate RIF1 splicing regulators chosen for secondary screening by shRNA knockdown.

Sup. Fig. 3. RIF1-L and RIF1-S isoforms have similar activity in canonical measures of RIF1 function. (A) Western blot analysis of *RIF1*$^{+/+}$ U-2 OS cells and *RIF1*$^{-/-}$ U-2 OS cells stably

transfected with plasmid vectors encoding GFP, GFP-RIF1-L, or GFP-RIF1-S. α-GFP (Santa Cruz sc9996, 1:200) and α-RIF1 (Bethyl Laboratories A300-569A; 1:500) detected a band of ~300 kDa from *RIF1*$^{-/-}$:GFP-RIF1-S and *RIF1*$^{-/-}$:GFP-RIF1-L U-2 OS cells. Lamin B1 (Abcam ab16048, 1:2000) was included as loading control. (B) RIF1-L and RIF1-S are recruited to IR-induced foci with comparable efficiency. *RIF1*$^{-/-}$:GFP-RIF1-S and *RIF1*$^{-/-}$:GFP-RIF1-L U-2 OS cells were exposed to 10 Gy IR (3 h) and stained DAPI prior to imaging. (C) MCM4 (Santa Cruz sc28317, 1:100 dilution) hyperphosphorylation in *RIF1*$^{-/-}$ U-2 OS cells were rescued by stable expression of GFP-RIF1-S or GFP-RIF1-L. (D) RIF1^{CTD}-S and RIF1^{CTD}-L binds to antiparallel G4 quadruplex substrate with equal anistrophy *in vitro*.

Sup. Fig. 4. RIF1-L and RIF1-S rescued the DNA replication pattern defect of *RIF1*$^{-/-}$ U-2 OS cells. Asynchronous U-2 OS cells of the indicated genotypes were pulse-labeled with EdU for 20 min and scored for the presence of early, mid, or late EdU staining patterns, as depicted in panel (A). (B) Representative EdU incorporation patterns of *RIF1*$^{-/-}$:GFP-RIF1-S and *RIF1*$^{-/-}$:GFP-RIF1-L U-2 OS cells. Cells exhibiting a mid-S-phase EdU incorporation patterns are denoted by yellow arrow. (C) Quantification analysis of the percentage of cells in each S phase pattern as shown in (A) using a minimum of 100 cells. Note the lack of middle-S-phase replication patterns in *RIF1*$^{-/-}$ cells that were rescued by both RIF1-L and RIF1-S.

Sup. Fig. 5. Comparison of T and B cell development of *RIF1*$^{+/+}$ and *RIF1*$^{\Delta Ex32}$ mice. (A) B cell development in the bone marrow (BM) of *RIF1*$^{+/+}$ and *RIF1*$^{\Delta Ex32}$ mice. BM cells from the mice were stained with anti-B220 and anti-IgM, anti-CD43 or anti-CD25 antibodies. The percentages indicate B220^{+}IgM^{-} pro/pre-, B220^{+}IgM^{+} immature and B220^{hi}IgM^{+} mature B cells (Left), B220^{+}CD43^{+} pro- (Middle), and B220^{+}CD25^{+} pre-B cells (Right) in the gated live cells. (B) T cell development in the thymus of *RIF1*$^{+/+}$ and *RIF1*$^{\Delta Ex32}$ mice. Thymocytes from the mice were stained with anti-CD4 and anti-CD8. The percentages indicate DN, DP, CD4 and CD8 T cells in the gated live cells. (C) B and T cell populations in the spleens of *RIF1*$^{+/+}$ and *RIF1*$^{\Delta Ex32}$ mice. Splenocytes from the mice were stained with anti-B220 and anti-Thy1.2. The percentages indicate B and T cells in the gated live cells. (D) T cell subpopulations in the spleen of *RIF1*$^{+/+}$ and *RIF1*$^{\Delta Ex32}$ mice. Splenocytes from the mice were stained with anti-CD4, anti-CD8, anti-CD62L and CD44. The percentages indicate CD4 and CD8 T cells in the gated live cells and CD62L^{hi}CD44^{lo} naïve, CD62L^{lo}CD44^{hi} effect memory, and CD62L^{hi}CD44^{hi} central memory T cells in the gated CD4^{+} or CD8^{+} cells. (E) TCR-induced thymidine incorporation in *RIF1*$^{+/+}$ and *RIF1*$^{\Delta Ex32}$ T cells. Splenic CD4 and CD8 T cells sorted from the mice were stimulated with medium, anti-CD3, anti-CD3 plus IL-2, anti-CD3 plus anti-CD28, or PMA plus Ionomycin. Proliferative responses were determined by [^{3}H]thymidine incorporation. (F) BCR-induced thymidine incorporation in *RIF1*$^{+/+}$ and *RIF1*$^{\Delta Ex32}$ B cells. Splenic B cells sorted from the mice were stimulated with medium, anti-IgM, or anti-IgM plus IL-4, anti-CD40, LPS, or PMA plus Ionomycin. Proliferative responses were determined by [^{3}H]thymidine incorporation. The data were obtained from 2 pairs of *RIF1*$^{+/+}$ and *RIF1*$^{\Delta Ex32}$ mice.

Sup. Fig. 6. Comparison of IgG class switch recombination **(CSR) potential of *RIF1*$^{+/+}$ and *RIF1*$^{\Delta Ex32}$ mice.** (A,B) Splenic B cells from *RIF1*$^{+/+}$ and *RIF1*$^{\Delta Ex32}$ mice stimulated for 4 days with CD40 plus IL-4 or LPS plus IL-4 were analyzed for *in vitro* CSR by FACS for IgG1 (A) and IgG2a (B). Percentages indicate cells in the gated B220^{+} population. (C,D) Splenic B cells from *RIF1*$^{+/+}$ and *RIF1*$^{\Delta Ex32}$ mice stimulated for 4 days with LPS were analyzed for *in vitro* CSR by FACS for IgG2b (C) and IgG3 (D). Percentages indicate cells in the gated B220^{+} population. The data were obtained from 2 pairs of *RIF1*$^{+/+}$ and *RIF1*$^{\Delta Ex32}$ mice.

Sup. Fig. 7. Lys residues in the S/K motif and CR2 confer microtubule association. (A) Schematic of GFP-tagged RIF1^{CTD}-L construct showing the two K/R-rich motifs within Ex32- and Ex34-encoded peptides. The right inset showed the alignment of these two motifs. Five selected Lys residues within S/K cassette and four selected Lys residues within the CR2 region which were subsequently mutated to Arg or Gln were marked. A double Phe to Leu mutant was included as negative control. (B) U-2 OS cells transiently transfected with the indicated GFP-RIF1 CTD constructs and stained with α-tubulin (Sigma T6199, 1:500). Note the presence of elaborated ribbon-like microtubule structures with abnormal nuclei on the left panel for GFP-RIF1^{CTD}-L, but this phenomenon was not observed in GFP-RIF1^{CTD}-S, and the Lys to Gln mutants of GFP-RIF1^{CTD}-L on the right panel. Scale bar = 10 μm. (C) Irradiated *RIF1*$^{-/-}$:GFP-RIF1-S and *RIF1*$^{-/-}$:GFP-RIF1-L U-2 OS cells were stained with anti-α-tubulin to visualize the colocalization of RIF1 and microtubules. Scale bar = 10 μm. Enlarged image of the white boxes were shown with a scale bar of 1 μm.

REFERENCES

Uncategorized References

1. Hardy, C.F., Sussel, L., and Shore, D. (1992). A RAP1-interacting protein involved in transcriptional silencing and telomere length regulation. Genes Dev *6*, 801-814. 10.1101/gad.6.5.801.
2. Mattarocci, S., Hafner, L., Lezaja, A., Shyian, M., and Shore, D. (2016). Rif1: A Conserved Regulator of DNA Replication and Repair Hijacked by Telomeres in Yeasts. Front Genet *7*, 45. 10.3389/fgene.2016.00045.
3. Chapman, J.R., Taylor, M.R., and Boulton, S.J. (2012). Playing the end game: DNA double-strand break repair pathway choice. Mol Cell *47*, 497-510. S1097-2765(12)00656-9 [pii]
10.1016/j.molcel.2012.07.029.
4. Chapman, J.R., Barral, P., Vannier, J.B., Borel, V., Steger, M., Tomas-Loba, A., Sartori, A.A., Adams, I.R., Batista, F.D., and Boulton, S.J. (2013). RIF1 is essential for 53BP1-dependent nonhomologous end joining and suppression of DNA double-strand break resection. Mol Cell *49*, 858-871. 10.1016/j.molcel.2013.01.002.
5. Zimmermann, M., and de Lange, T. (2014). 53BP1: pro choice in DNA repair. Trends Cell Biol *24*, 108-117. 10.1016/j.tcb.2013.09.003.
6. Escribano-Diaz, C., Orthwein, A., Fradet-Turcotte, A., Xing, M., Young, J.T., Tkac, J., Cook, M.A., Rosebrock, A.P., Munro, M., Canny, M.D., et al. (2013). A cell cycle-dependent regulatory circuit composed of 53BP1-RIF1 and BRCA1-CtIP controls DNA repair pathway choice. Mol Cell *49*, 872-883. 10.1016/j.molcel.2013.01.001.
7. Di Virgilio, M., Callen, E., Yamane, A., Zhang, W., Jankovic, M., Gitlin, A.D., Feldhahn, N., Resch, W., Oliveira, T.Y., Chait, B.T., et al. (2013). Rif1 prevents resection of DNA breaks and promotes immunoglobulin class switching. Science *339*, 711-715. 10.1126/science.1230624.
8. Dev, H., Chiang, T.W., Lescale, C., de Krijger, I., Martin, A.G., Pilger, D., Coates, J., Sczaniecka-Clift, M., Wei, W., Ostermaier, M., et al. (2018). Shieldin complex promotes DNA end-joining and counters homologous recombination in BRCA1-null cells. Nat Cell Biol *20*, 954-965. 10.1038/s41556-018-0140-1.
9. Gupta, R., Somyajit, K., Narita, T., Maskey, E., Stanlie, A., Kremer, M., Typas, D., Lammers, M., Mailand, N., Nussenzweig, A., et al. (2018). DNA Repair Network Analysis Reveals Shieldin as a Key Regulator of NHEJ and PARP Inhibitor Sensitivity. Cell *173*, 972-988 e923. 10.1016/j.cell.2018.03.050.
10. Mirman, Z., Lottersberger, F., Takai, H., Kibe, T., Gong, Y., Takai, K., Bianchi, A., Zimmermann, M., Durocher, D., and de Lange, T. (2018). 53BP1-RIF1-shieldin counteracts DSB resection through CST- and Polalpha-dependent fill-in. Nature *560*, 112-116. 10.1038/s41586-018-0324-7.
11. Noordermeer, S.M., Adam, S., Setiaputra, D., Barazas, M., Pettitt, S.J., Ling, A.K., Olivieri, M., Alvarez-Quilon, A., Moatti, N., Zimmermann, M., et al. (2018). The shieldin complex mediates 53BP1-dependent DNA repair. Nature *560*, 117-121. 10.1038/s41586-018-0340-7.
12. Zimmermann, M., Lottersberger, F., Buonomo, S.B., Sfeir, A., and de Lange, T. (2013). 53BP1 regulates DSB repair using Rif1 to control 5' end resection. Science *339*, 700-704. 10.1126/science.1231573.
13. Bouwman, P., Aly, A., Escandell, J.M., Pieterse, M., Bartkova, J., van der Gulden, H., Hiddingh, S., Thanasoula, M., Kulkarni, A., Yang, Q., et al. (2010). 53BP1 loss rescues BRCA1 deficiency and is associated with triple-negative and BRCA-mutated breast cancers. Nat Struct Mol Biol *17*, 688-695. 10.1038/nsmb.1831.

14. Bunting, S.F., Callen, E., Wong, N., Chen, H.T., Polato, F., Gunn, A., Bothmer, A., Feldhahn, N., Fernandez-Capetillo, O., Cao, L., et al. (2010). 53BP1 inhibits homologous recombination in Brca1-deficient cells by blocking resection of DNA breaks. Cell *141*, 243-254. 10.1016/j.cell.2010.03.012.
15. Xu, D., Muniandy, P., Leo, E., Yin, J., Thangavel, S., Shen, X., Ii, M., Agama, K., Guo, R., Fox, D., 3rd, et al. (2010). Rif1 provides a new DNA-binding interface for the Bloom syndrome complex to maintain normal replication. EMBO J *29*, 3140-3155. 10.1038/emboj.2010.186.
16. Hiraga, S.I., Ly, T., Garzon, J., Horejsi, Z., Ohkubo, Y.N., Endo, A., Obuse, C., Boulton, S.J., Lamond, A.I., and Donaldson, A.D. (2017). Human RIF1 and protein phosphatase 1 stimulate DNA replication origin licensing but suppress origin activation. EMBO Rep *18*, 403-419. 10.15252/embr.201641983.
17. Silverman, J., Takai, H., Buonomo, S.B., Eisenhaber, F., and de Lange, T. (2004). Human Rif1, ortholog of a yeast telomeric protein, is regulated by ATM and 53BP1 and functions in the S-phase checkpoint. Genes Dev *18*, 2108-2119. 10.1101/gad.1216004.
18. Buonomo, S.B., Wu, Y., Ferguson, D., and de Lange, T. (2009). Mammalian Rif1 contributes to replication stress survival and homology-directed repair. J Cell Biol *187*, 385-398. 10.1083/jcb.200902039.
19. Fragkos, M., Ganier, O., Coulombe, P., and Mechali, M. (2015). DNA replication origin activation in space and time. Nat Rev Mol Cell Biol *16*, 360-374. 10.1038/nrm4002.
20. Yamazaki, S., Ishii, A., Kanoh, Y., Oda, M., Nishito, Y., and Masai, H. (2012). Rif1 regulates the replication timing domains on the human genome. EMBO J *31*, 3667-3677. 10.1038/emboj.2012.180.
21. Cornacchia, D., Dileep, V., Quivy, J.P., Foti, R., Tili, F., Santarella-Mellwig, R., Antony, C., Almouzni, G., Gilbert, D.M., and Buonomo, S.B. (2012). Mouse Rif1 is a key regulator of the replication-timing programme in mammalian cells. EMBO J *31*, 3678-3690. 10.1038/emboj.2012.214.
22. Hayano, M., Kanoh, Y., Matsumoto, S., Renard-Guillet, C., Shirahige, K., and Masai, H. (2012). Rif1 is a global regulator of timing of replication origin firing in fission yeast. Genes Dev *26*, 137-150. 10.1101/gad.178491.111.
23. Kumar, R., and Cheok, C.F. (2014). RIF1: a novel regulatory factor for DNA replication and DNA damage response signaling. DNA Repair (Amst) *15*, 54-59. 10.1016/j.dnarep.2013.12.004.
24. Foti, R., Gnan, S., Cornacchia, D., Dileep, V., Bulut-Karslioglu, A., Diehl, S., Buness, A., Klein, F.A., Huber, W., Johnstone, E., et al. (2016). Nuclear Architecture Organized by Rif1 Underpins the Replication-Timing Program. Mol Cell *61*, 260-273. 10.1016/j.molcel.2015.12.001.
25. Gnan, S., Flyamer, I.M., Klein, K.N., Castelli, E., Rapp, A., Maiser, A., Chen, N., Weber, P., Enervald, E., Cardoso, M.C., et al. (2021). Nuclear organisation and replication timing are coupled through RIF1-PP1 interaction. Nat Commun *12*, 2910. 10.1038/s41467-021-22899-2.
26. Hengeveld, R.C., de Boer, H.R., Schoonen, P.M., de Vries, E.G., Lens, S.M., and van Vugt, M.A. (2015). Rif1 Is Required for Resolution of Ultrafine DNA Bridges in Anaphase to Ensure Genomic Stability. Dev Cell *34*, 466-474. 10.1016/j.devcel.2015.06.014.
27. Kong, N., Liu, Z., and Chan, Y.W. (2023). RIF1 suppresses the formation of single-stranded ultrafine anaphase bridges via protein phosphatase 1. Cell Rep *42*, 112032. 10.1016/j.celrep.2023.112032.
28. Watts, L.P., Natsume, T., Saito, Y., Garzon, J., Dong, Q., Boteva, L., Gilbert, N., Kanemaki, M.T., Hiraga, S.I., and Donaldson, A.D. (2020). The RIF1-long splice variant promotes G1 phase 53BP1 nuclear bodies to protect against replication stress. Elife *9*. 10.7554/eLife.58020.

29. Jia, W., Kim, S.H., Scalf, M.A., Tonzi, P., Millikin, R.J., Guns, W.M., Liu, L., Mastrocola, A.S., Smith, L.M., Huang, T.T., and Tibbetts, R.S. (2021). Fused in sarcoma regulates DNA replication timing and kinetics. J Biol Chem *297*, 101049. 10.1016/j.jbc.2021.101049.
30. Ran, F.A., Hsu, P.D., Lin, C.Y., Gootenberg, J.S., Konermann, S., Trevino, A.E., Scott, D.A., Inoue, A., Matoba, S., Zhang, Y., and Zhang, F. (2013). Double nicking by RNA-guided CRISPR Cas9 for enhanced genome editing specificity. Cell *154*, 1380-1389. 10.1016/j.cell.2013.08.021.
31. Ran, F.A., Hsu, P.D., Wright, J., Agarwala, V., Scott, D.A., and Zhang, F. (2013). Genome engineering using the CRISPR-Cas9 system. Nat Protoc *8*, 2281-2308. 10.1038/nprot.2013.143.
32. Kim, S.H., Zhan, L., Hanson, K.A., and Tibbetts, R.S. (2012). High-content RNAi screening identifies the Type 1 inositol triphosphate receptor as a modifier of TDP-43 localization and neurotoxicity. Hum Mol Genet. dds321 [pii]
10.1093/hmg/dds321.
33. Mastrocola, A.S., Kim, S.H., Trinh, A.T., Rodenkirch, L.A., and Tibbetts, R.S. (2013). The RNA-binding protein fused in sarcoma (FUS) functions downstream of poly(ADP-ribose) polymerase (PARP) in response to DNA damage. J Biol Chem *288*, 24731-24741. M113.497974 [pii]
10.1074/jbc.M113.497974.
34. Mohammed, H., Taylor, C., Brown, G.D., Papachristou, E.K., Carroll, J.S., and D'Santos, C.S. (2016). Rapid immunoprecipitation mass spectrometry of endogenous proteins (RIME) for analysis of chromatin complexes. Nat Protoc *11*, 316-326. 10.1038/nprot.2016.020.
35. Wisniewski, J.R., Zougman, A., Nagaraj, N., and Mann, M. (2009). Universal sample preparation method for proteome analysis. Nat Methods *6*, 359-362. 10.1038/nmeth.1322.
36. Sinitcyn, P., Richards, A.L., Weatheritt, R.J., Brademan, D.R., Marx, H., Shishkova, E., Meyer, J.G., Hebert, A.S., Westphall, M.S., and Blencowe, B.J. (2023). Global detection of human variants and isoforms by deep proteome sequencing. Nature biotechnology *41*, 1776-1786.
37. Shortreed, M.R., Wenger, C.D., Frey, B.L., Sheynkman, G.M., Scalf, M., Keller, M.P., Attie, A.D., and Smith, L.M. (2015). Global Identification of Protein Post-translational Modifications in a Single-Pass Database Search. J Proteome Res *14*, 4714-4720. 10.1021/acs.jproteome.5b00599.
38. Solntsev, S.K., Shortreed, M.R., Frey, B.L., and Smith, L.M. (2018). Enhanced Global Post-translational Modification Discovery with MetaMorpheus. J Proteome Res *17*, 1844-1851. 10.1021/acs.jproteome.7b00873.
39. Millikin, R.J., Solntsev, S.K., Shortreed, M.R., and Smith, L.M. (2018). Ultrafast Peptide Label-Free Quantification with FlashLFQ. J Proteome Res *17*, 386-391. 10.1021/acs.jproteome.7b00608.
40. Millikin, R.J., Shortreed, M.R., Scalf, M., and Smith, L.M. (2020). A Bayesian Null Interval Hypothesis Test Controls False Discovery Rates and Improves Sensitivity in Label-Free Quantitative Proteomics. J Proteome Res *19*, 1975-1981. 10.1021/acs.jproteome.9b00796.
41. Koulouras, G., Panagopoulos, A., Rapsomaniki, M.A., Giakoumakis, N.N., Taraviras, S., and Lygerou, Z. (2018). EasyFRAP-web: a web-based tool for the analysis of fluorescence recovery after photobleaching data. Nucleic Acids Res *46*, W467-W472. 10.1093/nar/gky508.
42. Guo, L., Kim, H.J., Wang, H., Monaghan, J., Freyermuth, F., Sung, J.C., O'Donovan, K., Fare, C.M., Diaz, Z., Singh, N., et al. (2018). Nuclear-Import Receptors Reverse

Aberrant Phase Transitions of RNA-Binding Proteins with Prion-like Domains. Cell *173*, 677-692 e620. 10.1016/j.cell.2018.03.002.

43. Zhang, Y., Lin, D., Zheng, Y., Chen, Y., Yu, M., Cui, D., Huang, M., Su, X., Sun, Y., Chen, Y., et al. (2023). MiR-9-1 controls osteoblastic regulation of lymphopoiesis. Leukemia *37*, 2261-2275. 10.1038/s41375-023-02014-8.
44. Zheng, Y., Yu, M., Podd, A., Yuan, L., Newman, D.K., Wen, R., Arepally, G., and Wang, D. (2013). Critical role for mouse marginal zone B cells in PF4/heparin antibody production. Blood *121*, 3484-3492. 10.1182/blood-2013-01-477091.
45. Setiaputra, D., Escribano-Diaz, C., Reinert, J.K., Sadana, P., Zong, D., Callen, E., Sifri, C., Seebacher, J., Nussenzweig, A., Thoma, N.H., and Durocher, D. (2022). RIF1 acts in DNA repair through phosphopeptide recognition of 53BP1. Mol Cell *82*, 1359-1371 e1359. 10.1016/j.molcel.2022.01.025.
46. Sukackaite, R., Jensen, M.R., Mas, P.J., Blackledge, M., Buonomo, S.B., and Hart, D.J. (2014). Structural and biophysical characterization of murine rif1 C terminus reveals high specificity for DNA cruciform structures. J Biol Chem *289*, 13903-13911. 10.1074/jbc.M114.557843.
47. Hiraga, S., Alvino, G.M., Chang, F., Lian, H.Y., Sridhar, A., Kubota, T., Brewer, B.J., Weinreich, M., Raghuraman, M.K., and Donaldson, A.D. (2014). Rif1 controls DNA replication by directing Protein Phosphatase 1 to reverse Cdc7-mediated phosphorylation of the MCM complex. Genes Dev *28*, 372-383. 10.1101/gad.231258.113.
48. Breitkreutz, A., Choi, H., Sharom, J.R., Boucher, L., Neduva, V., Larsen, B., Lin, Z.Y., Breitkreutz, B.J., Stark, C., Liu, G., et al. (2010). A global protein kinase and phosphatase interaction network in yeast. Science *328*, 1043-1046. 10.1126/science.1176495.
49. Sifri, C., Hoeg, L., Durocher, D., and Setiaputra, D. (2023). An AlphaFold2 map of the 53BP1 pathway identifies a direct SHLD3-RIF1 interaction critical for shieldin activity. EMBO Rep *24*, e56834. 10.15252/embr.202356834.
50. Vitting-Seerup, K., and Sandelin, A. (2017). The landscape of isoform switches in human cancers. Molecular Cancer Research *15*, 1206-1220.
51. Yu, T., Cazares, O., Tang, A.D., Kim, H.Y., Wald, T., Verma, A., Liu, Q., Barcellos-Hoff, M.H., Floor, S.N., Jung, H.S., et al. (2022). SRSF1 governs progenitor-specific alternative splicing to maintain adult epithelial tissue homeostasis and renewal. Dev Cell *57*, 624-637 e624. 10.1016/j.devcel.2022.01.011.
52. Pandit, S., Zhou, Y., Shiue, L., Coutinho-Mansfield, G., Li, H., Qiu, J., Huang, J., Yeo, G.W., Ares, M., Jr., and Fu, X.D. (2013). Genome-wide analysis reveals SR protein cooperation and competition in regulated splicing. Mol Cell *50*, 223-235. 10.1016/j.molcel.2013.03.001.
53. Cho, S., Hoang, A., Sinha, R., Zhong, X.Y., Fu, X.D., Krainer, A.R., and Ghosh, G. (2011). Interaction between the RNA binding domains of Ser-Arg splicing factor 1 and U1-70K snRNP protein determines early spliceosome assembly. Proc Natl Acad Sci U S A *108*, 8233-8238. 10.1073/pnas.1017700108.
54. Sanford, J.R., Wang, X., Mort, M., Vanduyn, N., Cooper, D.N., Mooney, S.D., Edenberg, H.J., and Liu, Y. (2009). Splicing factor SFRS1 recognizes a functionally diverse landscape of RNA transcripts. Genome Res *19*, 381-394. 10.1101/gr.082503.108.
55. Liu, H.X., Zhang, M., and Krainer, A.R. (1998). Identification of functional exonic splicing enhancer motifs recognized by individual SR proteins. Genes Dev *12*, 1998-2012. 10.1101/gad.12.13.1998.
56. Clery, A., Krepl, M., Nguyen, C.K.X., Moursy, A., Jorjani, H., Katsantoni, M., Okoniewski, M., Mittal, N., Zavolan, M., Sponer, J., and Allain, F.H. (2021). Structure of SRSF1 RRM1 bound to RNA reveals an unexpected bimodal mode of interaction and explains

its involvement in SMN1 exon7 splicing. Nat Commun *12*, 428. 10.1038/s41467-020-20481-w.

57. Dimitrova, D.S. (2002). The spatio-temporal organization of DNA replication sites is identical in primary, immortalized and transformed mammalian cells. Journal of Cell Science *115*, 4037-4051. 10.1242/jcs.00087.
58. Sukackaite, R., Cornacchia, D., Jensen, M.R., Mas, P.J., Blackledge, M., Enervald, E., Duan, G., Auchynnikava, T., Kohn, M., Hart, D.J., and Buonomo, S.B.C. (2017). Mouse Rif1 is a regulatory subunit of protein phosphatase 1 (PP1). Sci Rep *7*, 2119. 10.1038/s41598-017-01910-1.
59. Segura-Bayona, S., Knobel, P.A., Gonzalez-Buron, H., Youssef, S.A., Pena-Blanco, A., Coyaud, E., Lopez-Rovira, T., Rein, K., Palenzuela, L., Colombelli, J., et al. (2017). Differential requirements for Tousled-like kinases 1 and 2 in mammalian development. Cell Death Differ *24*, 1872-1885. 10.1038/cdd.2017.108.
60. Tang, M., Chen, Z., Wang, C., Feng, X., Lee, N., Huang, M., Zhang, H., Li, S., Xiong, Y., and Chen, J. (2022). Histone chaperone ASF1 acts with RIF1 to promote DNA end joining in BRCA1-deficient cells. J Biol Chem *298*, 101979. 10.1016/j.jbc.2022.101979.
61. Feng, S., Ma, S., Li, K., Gao, S., Ning, S., Shang, J., Guo, R., Chen, Y., Blumenfeld, B., Simon, I., et al. (2022). RIF1-ASF1-mediated high-order chromatin structure safeguards genome integrity. Nat Commun *13*, 957. 10.1038/s41467-022-28588-y.
62. Kumagai, A., and Dunphy, W.G. (2000). Claspin, a novel protein required for the activation of Chk1 during a DNA replication checkpoint response in Xenopus egg extracts. Mol Cell *6*, 839-849. 10.1016/s1097-2765(05)00092-4.
63. Smits, V.A.J., Cabrera, E., Freire, R., and Gillespie, D.A. (2019). Claspin - checkpoint adaptor and DNA replication factor. FEBS J *286*, 441-455. 10.1111/febs.14594.
64. Peng, A., and Chen, P.L. (2003). NFBD1, like 53BP1, is an early and redundant transducer mediating Chk2 phosphorylation in response to DNA damage. J Biol Chem *278*, 8873-8876. 10.1074/jbc.C300001200.
65. Goldberg, M., Stucki, M., Falck, J., D'Amours, D., Rahman, D., Pappin, D., Bartek, J., and Jackson, S.P. (2003). MDC1 is required for the intra-S-phase DNA damage checkpoint. Nature *421*, 952-956. 10.1038/nature01445.
66. Lou, Z., Minter-Dykhouse, K., Wu, X., and Chen, J. (2003). MDC1 is coupled to activated CHK2 in mammalian DNA damage response pathways. Nature *421*, 957-961. 10.1038/nature01447.
67. Stewart, G.S., Wang, B., Bignell, C.R., Taylor, A.M., and Elledge, S.J. (2003). MDC1 is a mediator of the mammalian DNA damage checkpoint. Nature *421*, 961-966. 10.1038/nature01446.
68. Xu, X., and Stern, D.F. (2003). NFBD1/KIAA0170 is a chromatin-associated protein involved in DNA damage signaling pathways. J Biol Chem *278*, 8795-8803. 10.1074/jbc.M211392200.
69. Gursoy-Yuzugullu, O., Ayrapetov, M.K., and Price, B.D. (2015). Histone chaperone Anp32e removes H2A.Z from DNA double-strand breaks and promotes nucleosome reorganization and DNA repair. Proc Natl Acad Sci U S A *112*, 7507-7512. 10.1073/pnas.1504868112.
70. Cheng, L., Yuan, B., Ying, S., Niu, C., Mai, H., Guan, X., Yang, X., Teng, Y., Lin, J., Huang, J., et al. (2019). PES1 is a critical component of telomerase assembly and regulates cellular senescence. Sci Adv *5*, eaav1090. 10.1126/sciadv.aav1090.
71. Chao, W.C., Kulkarni, K., Zhang, Z., Kong, E.H., and Barford, D. (2012). Structure of the mitotic checkpoint complex. Nature *484*, 208-213. 10.1038/nature10896.
72. Sudakin, V., Chan, G.K., and Yen, T.J. (2001). Checkpoint inhibition of the APC/C in HeLa cells is mediated by a complex of BUBR1, BUB3, CDC20, and MAD2. J Cell Biol *154*, 925-936. 10.1083/jcb.200102093.

73. Ochi, T., Blackford, A.N., Coates, J., Jhujh, S., Mehmood, S., Tamura, N., Travers, J., Wu, Q., Draviam, V.M., Robinson, C.V., et al. (2015). DNA repair. PAXX, a paralog of XRCC4 and XLF, interacts with Ku to promote DNA double-strand break repair. Science *347*, 185-188. 10.1126/science.1261971.
74. Huen, M.S., Grant, R., Manke, I., Minn, K., Yu, X., Yaffe, M.B., and Chen, J. (2007). RNF8 transduces the DNA-damage signal via histone ubiquitylation and checkpoint protein assembly. Cell *131*, 901-914. 10.1016/j.cell.2007.09.041.
75. Mailand, N., Bekker-Jensen, S., Faustrup, H., Melander, F., Bartek, J., Lukas, C., and Lukas, J. (2007). RNF8 ubiquitylates histones at DNA double-strand breaks and promotes assembly of repair proteins. Cell *131*, 887-900. 10.1016/j.cell.2007.09.040.
76. Kolas, N.K., Chapman, J.R., Nakada, S., Ylanko, J., Chahwan, R., Sweeney, F.D., Panier, S., Mendez, M., Wildenhain, J., Thomson, T.M., et al. (2007). Orchestration of the DNA-damage response by the RNF8 ubiquitin ligase. Science *318*, 1637-1640. 10.1126/science.1150034.
77. Moiseeva, T.N., Qian, C., Sugitani, N., Osmanbeyoglu, H.U., and Bakkenist, C.J. (2019). WEE1 kinase inhibitor AZD1775 induces CDK1 kinase-dependent origin firing in unperturbed G1- and S-phase cells. Proc Natl Acad Sci U S A *116*, 23891-23893. 10.1073/pnas.1915108116.
78. Moiseeva, T.N., Yin, Y., Calderon, M.J., Qian, C., Schamus-Haynes, S., Sugitani, N., Osmanbeyoglu, H.U., Rothenberg, E., Watkins, S.C., and Bakkenist, C.J. (2019). An ATR and CHK1 kinase signaling mechanism that limits origin firing during unperturbed DNA replication. Proc Natl Acad Sci U S A *116*, 13374-13383. 10.1073/pnas.1903418116.
79. Jones, D.T., and Cozzetto, D. (2015). DISOPRED3: precise disordered region predictions with annotated protein-binding activity. Bioinformatics *31*, 857-863. 10.1093/bioinformatics/btu744.
80. Yu, H., Lu, S., Gasior, K., Singh, D., Vazquez-Sanchez, S., Tapia, O., Toprani, D., Beccari, M.S., Yates, J.R., 3rd, Da Cruz, S., et al. (2021). HSP70 chaperones RNA-free TDP-43 into anisotropic intranuclear liquid spherical shells. Science *371*. 10.1126/science.abb4309.
81. Alberti, S., Gladfelter, A., and Mittag, T. (2019). Considerations and Challenges in Studying Liquid-Liquid Phase Separation and Biomolecular Condensates. Cell *176*, 419-434. 10.1016/j.cell.2018.12.035.
82. Subramanian, R., Wilson-Kubalek, E.M., Arthur, C.P., Bick, M.J., Campbell, E.A., Darst, S.A., Milligan, R.A., and Kapoor, T.M. (2010). Insights into antiparallel microtubule crosslinking by PRC1, a conserved nonmotor microtubule binding protein. Cell *142*, 433-443. 10.1016/j.cell.2010.07.012.
83. Mollinari, C., Kleman, J.P., Jiang, W., Schoehn, G., Hunter, T., and Margolis, R.L. (2002). PRC1 is a microtubule binding and bundling protein essential to maintain the mitotic spindle midzone. J Cell Biol *157*, 1175-1186. 10.1083/jcb.200111052.
84. Yu, T., Cazares, O., Tang, A.D., Kim, H.-Y., Wald, T., Verma, A., Liu, Q., Barcellos-Hoff, M.H., Floor, S.N., and Jung, H.-S. (2022). SRSF1 governs progenitor-specific alternative splicing to maintain adult epithelial tissue homeostasis and renewal. Developmental Cell *57*, 624-637. e624.
85. Xiao, R., Sun, Y., Ding, J.-H., Lin, S., Rose, D.W., Rosenfeld, M.G., Fu, X.-D., and Li, X. (2007). Splicing regulator SC35 is essential for genomic stability and cell proliferation during mammalian organogenesis. Molecular and cellular biology *27*, 5393-5402.
86. Li, S., Huang, X., Zheng, S., Zhang, W., Liu, F., and Cao, Q. (2024). High expression of SRSF1 facilitates osteosarcoma progression and unveils its potential mechanisms. BMC cancer *24*, 580.

87. Salguero, I., Belotserkovskaya, R., Coates, J., Sczaniecka-Clift, M., Demir, M., Jhujh, S., Wilson, M.D., and Jackson, S.P. (2019). MDC1 PST-repeat region promotes histone H2AX-independent chromatin association and DNA damage tolerance. Nat Commun *10*, 5191. 10.1038/s41467-019-12929-5.
88. Wang, J., Choi, J.-M., Holehouse, A.S., Lee, H.O., Zhang, X., Jahnel, M., Maharana, S., Lemaitre, R., Pozniakovsky, A., and Drechsel, D. (2018). A molecular grammar governing the driving forces for phase separation of prion-like RNA binding proteins. Cell *174*, 688-699. e616.
89. Oropesa-Ávila, M., Fernández-Vega, A., de La Mata, M., Maraver, J., Cordero, M.D., Cotán, D., De Miguel, M., Calero, C., Paz, M., and Pavón, A. (2013). Apoptotic microtubules delimit an active caspase free area in the cellular cortex during the execution phase of apoptosis. Cell death & disease *4*, e527-e527.
90. Ustinova, K., Novakova, Z., Saito, M., Meleshin, M., Mikesova, J., Kutil, Z., Baranova, P., Havlinova, B., Schutkowski, M., Matthias, P., and Barinka, C. (2020). The disordered N-terminus of HDAC6 is a microtubule-binding domain critical for efficient tubulin deacetylation. J Biol Chem *295*, 2614-2628. 10.1074/jbc.RA119.011243.
91. Janke, C. (2014). The tubulin code: molecular components, readout mechanisms, and functions. J Cell Biol *206*, 461-472. 10.1083/jcb.201406055.
92. Xu, L., and Blackburn, E.H. (2004). Human Rif1 protein binds aberrant telomeres and aligns along anaphase midzone microtubules. J Cell Biol *167*, 819-830. 10.1083/jcb.200408181.
93. Shokrollahi, M., and Mekhail, K. (2021). Interphase microtubules in nuclear organization and genome maintenance. Trends Cell Biol *31*, 721-731. 10.1016/j.tcb.2021.03.014.

Supplemental Figures

Koo *et al.* Sup. Fig. 1

A

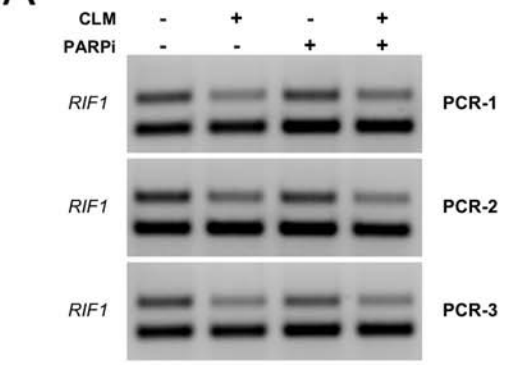

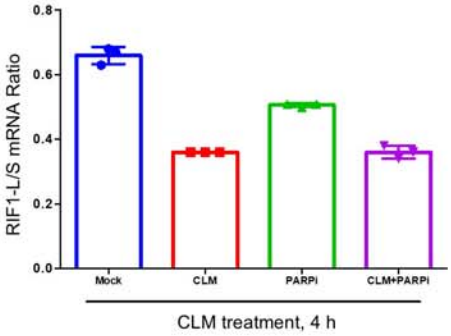

B

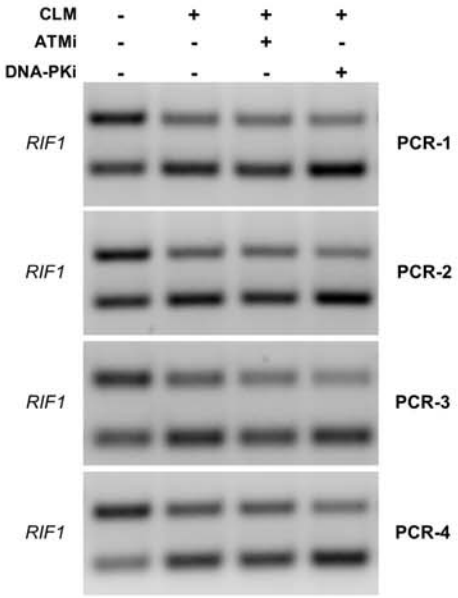

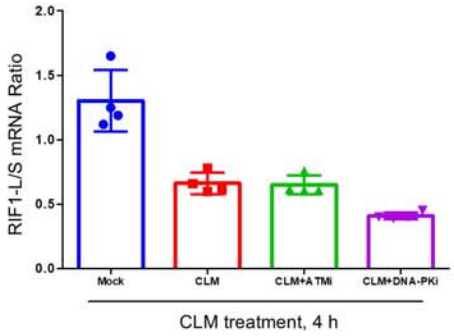

A

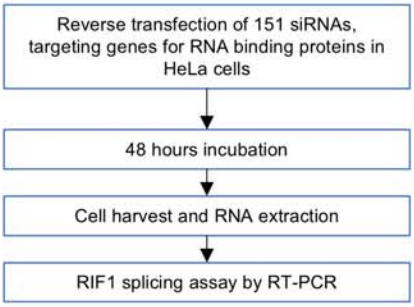

C

Sample ID	Target	RIF1-L/S ratio
NT	Non-targeting control	0.54
15	PTBP1	2.61
36	RBM28	1.33
83	SRSF1	0.16
93	snRNP70	0.25
95	SRSF7	1.5
110	SRSF3	2.83

B

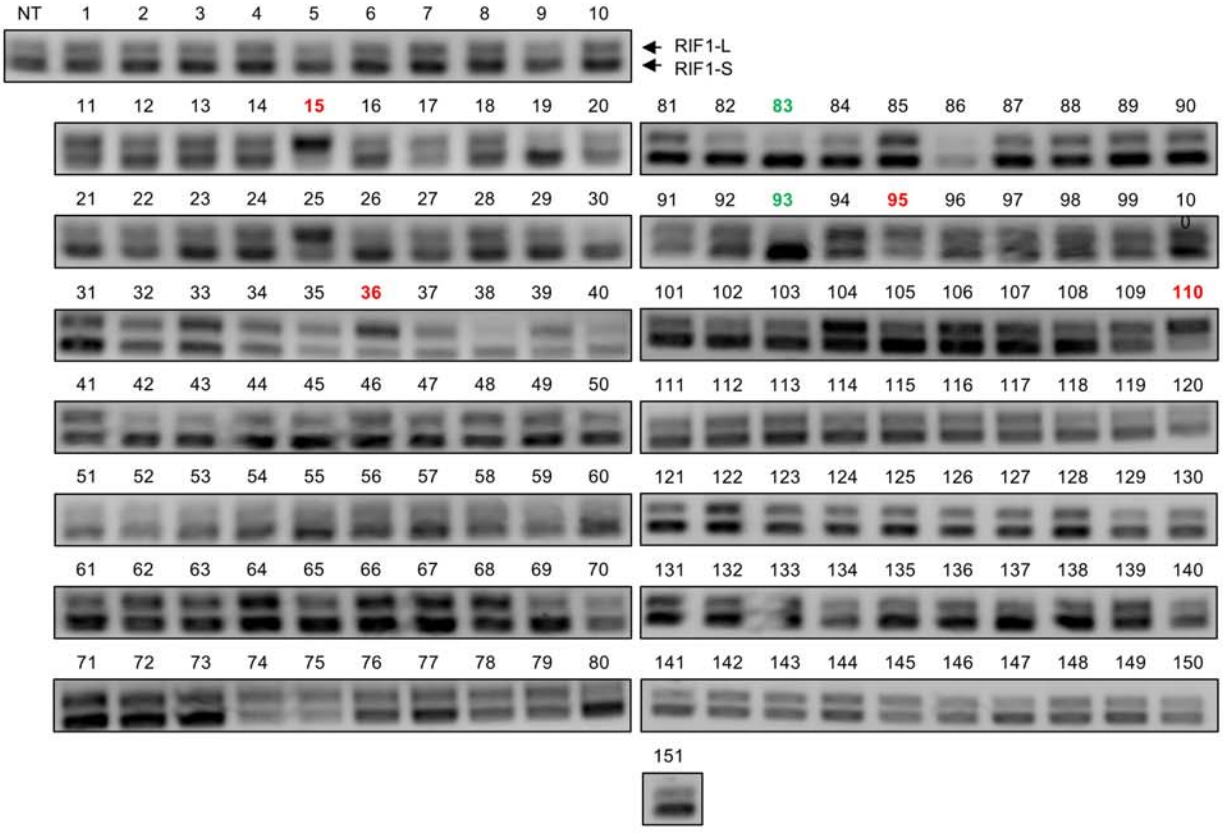

Koo *et al.* Sup. Fig. 3

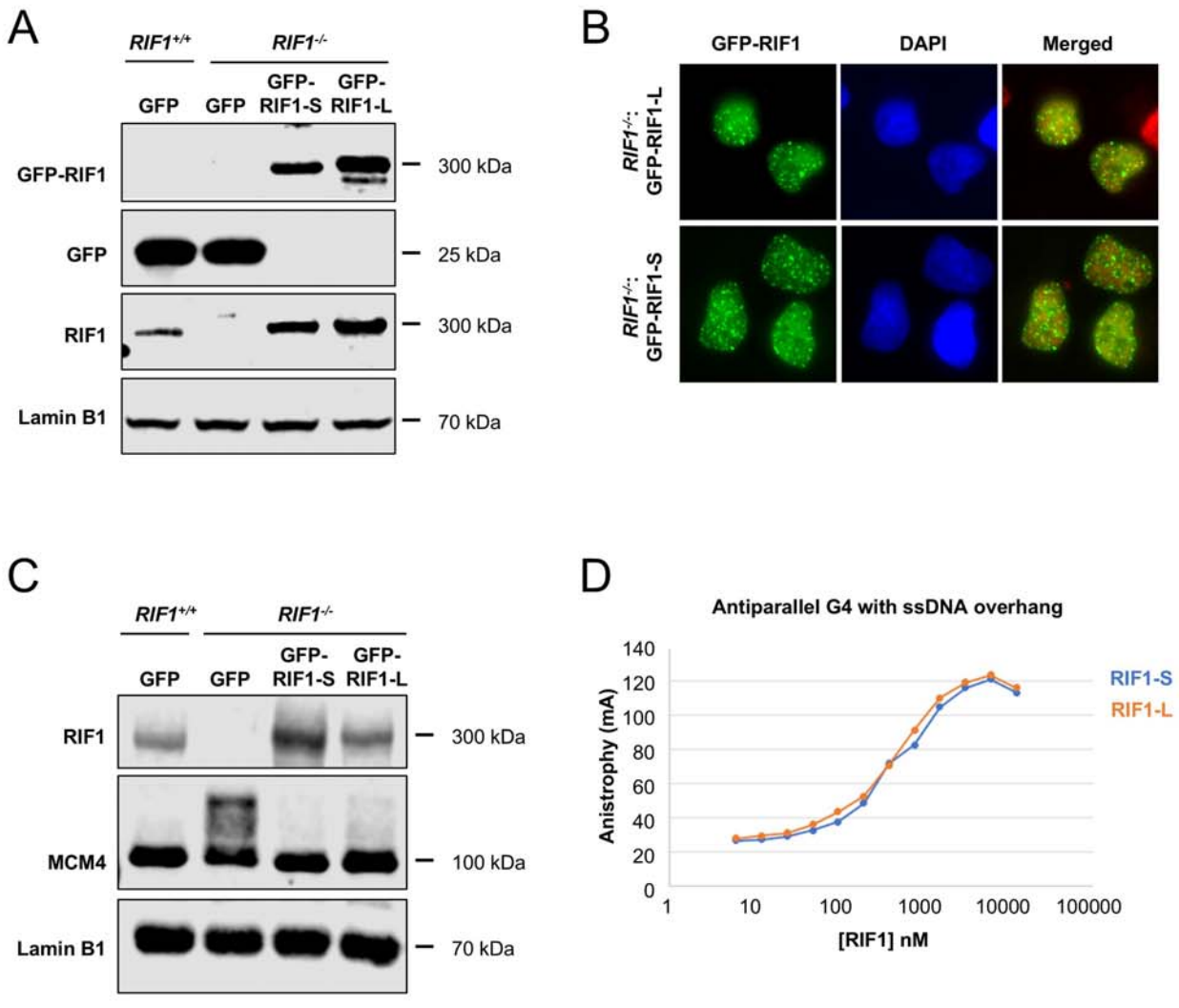

Koo *et al.* Sup. Fig. 4

A

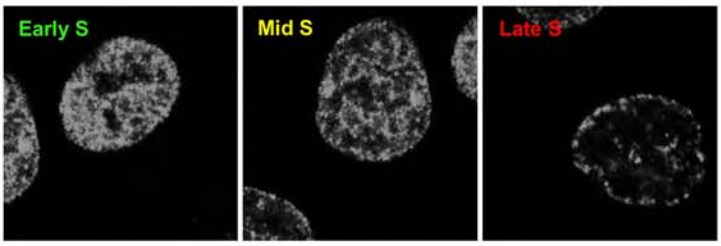

B

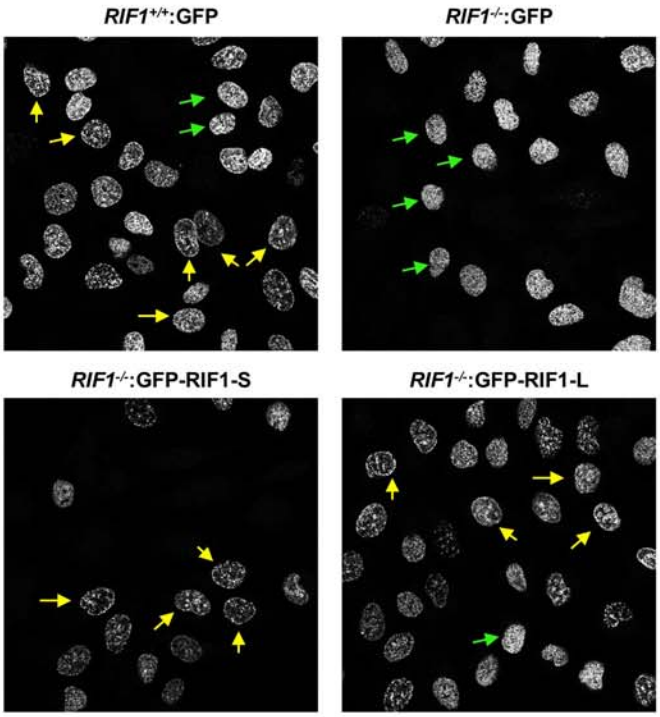

C

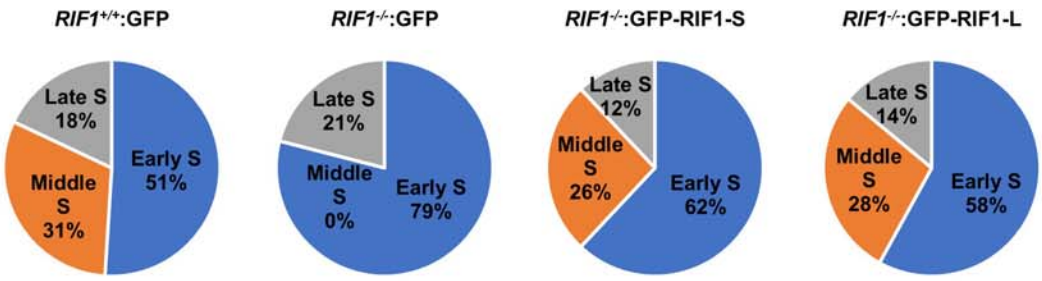

Koo *et al.* Sup. Fig. 5

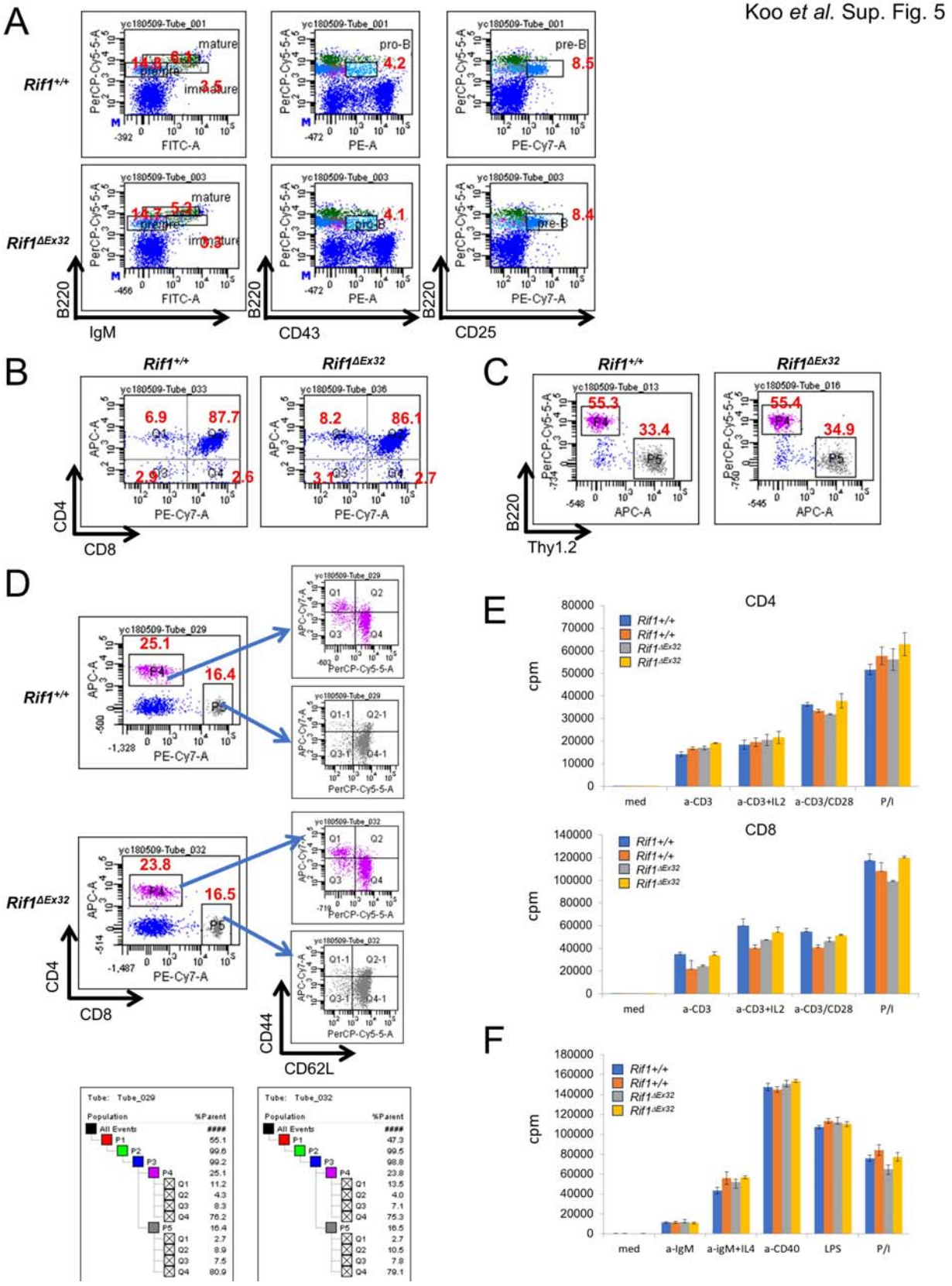

Koo *et al.* Sup. Fig. 6

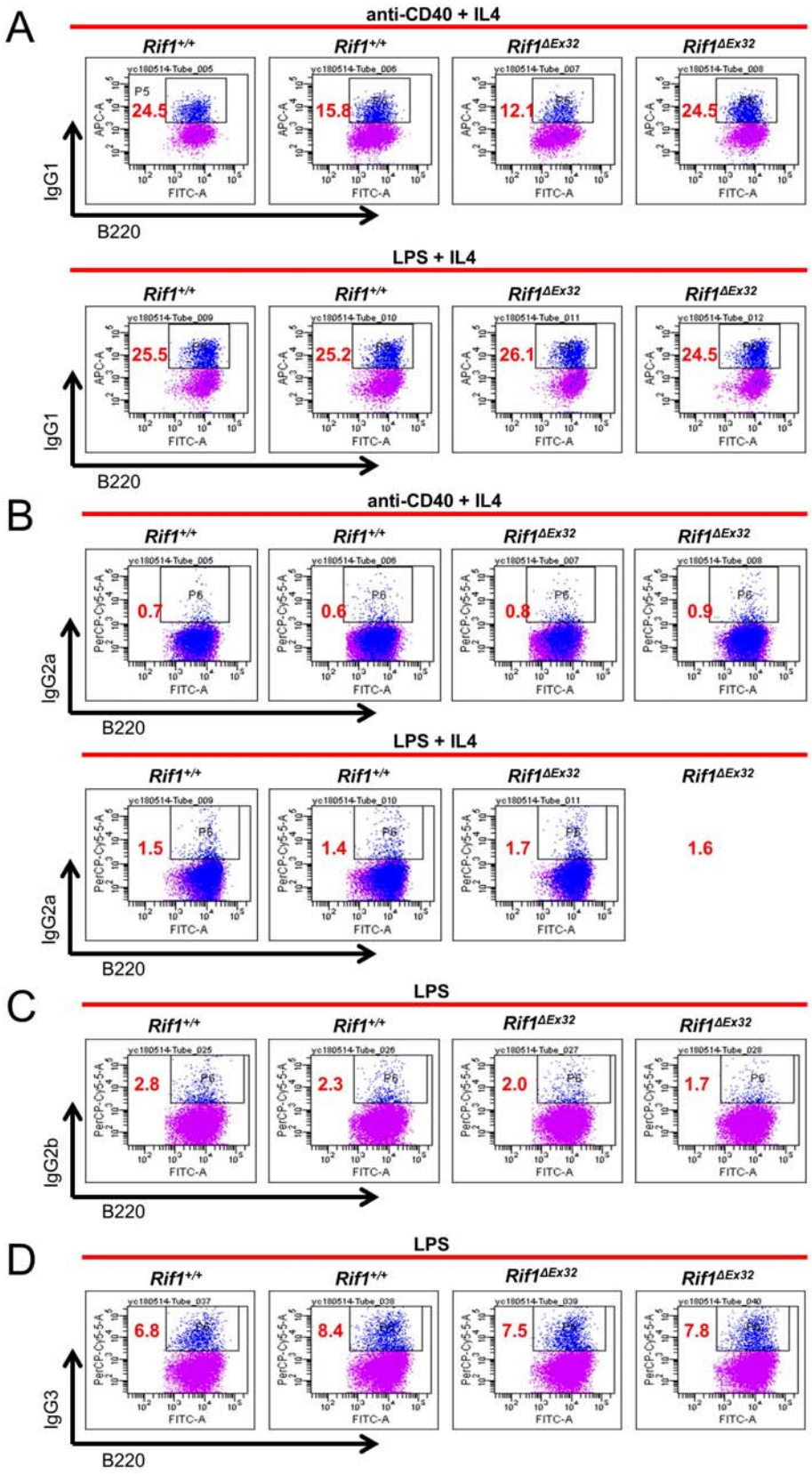

Koo *et al.* Sup. Fig. 7